Chapter 2
Bubble Dynamics

Abstract Bubble pulsation is mathematically described by the Rayleigh–Plesset equation and by Keller equation. Derivation of the equations is fully described herein. Using the Rayleigh–Plesset equation, the violent collapse of a bubble is discussed. A method of numerical simulations of bubble pulsation is also described. In relation to numerical simulations, non-equilibrium evaporation and condensation of water vapor at the bubble wall, the variation in liquid temperature at the bubble wall, the gas diffusion across the bubble wall, and the chemical reactions inside a bubble are discussed. Comparison between numerical results and experimental data for a single-bubble system is shown. The main oxidants created inside a bubble are described based upon numerical simulations data. Linear and nonlinear resonance radius of a bubble is discussed as well as the analytical solution of the linearized equation of bubble pulsation. The mechanism of shock wave emission from a bubble into surrounding liquid is discussed. Inside a collapsing bubble, a shock wave is seldom formed due to lower temperature near the bubble wall. A liquid jet penetrates into a collapsing bubble near the solid surface. The bubble pulsation is influenced by the acoustic emissions from the surrounding bubbles, which is called *bubble–bubble interaction*. The origin of acoustic cavitation noise is discussed based upon results of numerical simulations. It is shown that surfactants and salts strongly retard bubble–bubble coalescence.

Keywords Rayleigh–Plesset equation · Keller equation · Rayleigh collapse Resonance radius · Shock wave · Jetting · Primary and secondary Bjerkens forces · Bubble–bubble interaction · Acoustic cavitation noise · Acoustic streaming

2.1 Rayleigh–Plesset Equation

A typical cavitation bubble is filled with vapor and non-condensable gas such as air. The pressure inside a bubble is higher than the liquid pressure at the bubble wall due to surface tension [1, 2]. The surface tension (σ) is the surface energy per unit

K. Yasui, *Acoustic Cavitation and Bubble Dynamics*,
Ultrasound and Sonochemistry, https://doi.org/10.1007/978-3-319-68237-2_2

area and is 7.275×10^{-2} (N/m) (= J/m^2) for pure water at 20 °C. For a spherical bubble with a radius R, the surface energy is $4\pi\sigma R^2$ because the surface area is $4\pi R^2$. The work required to expand a bubble by dR in radius is $8\pi\sigma R\mathrm{d}R$ because the surface area becomes $4\pi(R + \mathrm{d}R)^2 = 4\pi R^2 + 8\pi R\mathrm{d}R$ [neglecting the $(\mathrm{d}R)^2$ term]. Thus, the force needed to expand a bubble is $8\pi\sigma R$ because the work is the force multiplied by the distance moved (dR). The balance between the force inside and outside a bubble is expressed as $4\pi R^2 p_{\mathrm{in}} = 4\pi R^2 p_{\mathrm{B}} + 8\pi\sigma R$, where p_{in} is the pressure inside the bubble, and p_{B} is the liquid pressure at the bubble wall. Thus, the following relationship holds.

$$p_{\mathrm{in}} = p_{\mathrm{B}} + \frac{2\sigma}{R} \tag{2.1}$$

The second term on the right side of Eq. (2.1) is called the *Laplace pressure*. The pressure inside a bubble is higher than the liquid pressure at the bubble wall by the Laplace pressure. In Fig. 2.1, the Laplace pressure is shown as a function of bubble radius in pure water at 20 °C. The Laplace pressure is 1.5 bar for R = 1 μm and increases as the bubble radius decreases. For R = 100 nm (= 0.1 μm), it is as high as 15 bar (= 1.5×10^6 Pa ≈ 15 atm) [3].

Bubble dynamics such as violent bubble collapse is crudely described by the Rayleigh–Plesset equation. In its derivation, a spherical liquid volume with radius R_{L} surrounding a spherical bubble with radius R is considered with the center of a liquid volume at the center of a spherical bubble (Fig. 2.2) [2]. The radius of the liquid volume is much smaller than the wavelength of ultrasound in liquid; $R_{\mathrm{L}} \ll \lambda$. When a bubble expands or collapses, the liquid volume also correspondingly expands or contracts, respectively. The kinetic energy of the liquid volume is estimated as follows: A spherical shell of liquid with thickness dr and radius r from the center of a spherical bubble has a kinetic energy of $1/2 \times 4\pi r^2 \rho_0 \mathrm{d}r$ (the mass) $\times$ $(\mathrm{d}r/\mathrm{d}t)^2$ (square of velocity), where ρ_0 is the equilibrium density of the liquid. The total

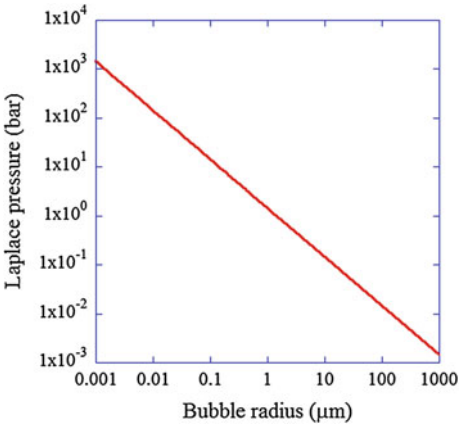

Fig. 2.1 Laplace pressure in pure water at 20 °C as a function of bubble radius [3]

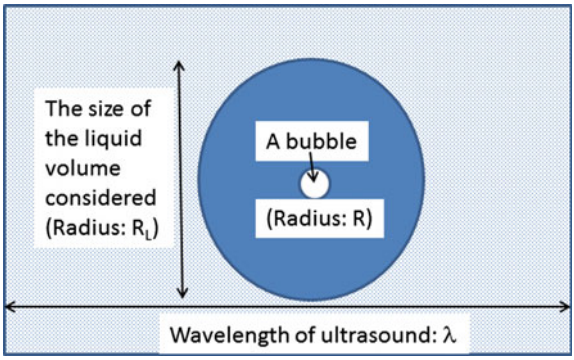

Fig. 2.2 Derivation of the Rayleigh–Plesset equation of bubble pulsation. Reprinted with permission from Yasui [2]. Copyright (2015), Elsevier

kinetic energy (E_K) of the liquid volume is the integration of the above quantity with respect to radius r from R to R_L, where R is the instantaneous bubble radius.

$$E_K = \frac{1}{2}\rho_0 \int_R^{R_L} \left(\frac{dr}{dt}\right)^2 4\pi r^2 dr = 2\pi\rho_0 R^3 \left(\frac{dR}{dt}\right)^2 \tag{2.2}$$

where the liquid is assumed to be incompressible $\left(4\pi r^2 \frac{dr}{dt} = 4\pi R^2 \frac{dr}{dt}\right)$, and $R \ll R_L$.

When a bubble expands, it does work on the surrounding liquid. When a bubble collapses, the surrounding liquid does work on a bubble. In other words, a bubble does negative work on the surrounding liquid. The work (W_{bubble}) done by a bubble to the surrounding liquid can be expressed as follows:

$$W_{bubble} = \int_{R_0}^{R} 4\pi r^2 p_B dr \tag{2.3}$$

where R_0 is the initial ambient bubble radius which is defined as the bubble radius in the absence of driving acoustic wave (ultrasound).

When a bubble expands, the liquid volume also expands. In other words, the liquid volume does work to the surrounding liquid. When a bubble collapses, the liquid volume contracts and does negative work on the surrounding liquid. The work (W_{liquid}) done by the liquid volume is expressed as follows.

$$W_{liquid} = p_\infty \Delta V = p_\infty \int_{R_0}^{R} 4\pi r^2 dr \tag{2.4}$$

where p_∞ is the pressure at the surface of the liquid volume which is assumed to be the ambient static pressure plus the instantaneous acoustic pressure. ΔV is the

volume swept by the liquid volume from the initial radius of R_L. Here, the liquid is assumed to be incompressible (The volume swept by a liquid is equivalent to the change in bubble volume.)

The conservation of energy yields the following relationship.

$$W_{\text{bubble}} = E_K + W_{\text{liquid}} \tag{2.5}$$

Equation (2.5) can now be differentiated with respect to R. Firstly, the differentiation of Eq. (2.3) yields Eq. (2.6).

$$\frac{\partial W_{\text{bubble}}}{\partial R} = 4\pi R^2 p_B \tag{2.6}$$

Secondly, the differentiation of Eq. (2.2) yields Eq. (2.7).

$$\frac{\partial E_K}{\partial R} = 6\pi\rho_0 R^2 \left(\frac{dR}{dt}\right)^2 + 4\pi\rho_0 R^3 \frac{d^2R}{dt^2} \tag{2.7}$$

where the following relationship has been used.

$$\frac{\partial}{\partial R}\left[\left(\frac{dR}{dt}\right)^2\right] = \frac{\partial\left(\dot{R}^2\right)}{\partial R} = \frac{1}{\dot{R}}\frac{\partial\left(\dot{R}^2\right)}{\partial t} = 2\ddot{R} = 2\frac{d^2R}{dt^2} \tag{2.8}$$

where "dot" denotes the time derivative (d/dt). Finally, the differentiation of Eq. (2.4) yields Eq. (2.9).

$$\frac{\partial W_{\text{liquid}}}{\partial R} = 4\pi R^2 p_\infty \tag{2.9}$$

From Eqs. (2.6), (2.7), and (2.9), differentiation of Eq. (2.5) with respect to R becomes Eq. (2.10).

$$\frac{p_B - p_\infty}{\rho_0} = \frac{3}{2}\dot{R}^2 + R\ddot{R} \tag{2.10}$$

When the bubble wall is moving, there is an additional term in Eq. (2.1) due to viscosity.

$$p_B = p_g + p_v - \frac{2\sigma}{R} - \frac{4\mu\dot{R}}{R} \tag{2.11}$$

where p_g and p_v are partial pressures of non-condensable gas and vapor, respectively, $\left(p_{in} = p_g + p_v\right)$, and μ is the liquid viscosity. In the derivation of the last term on right-hand side of Eq. (2.11), the incompressibility of liquid is assumed to be $4\pi r^2\dot{r} = 4\pi R^2\dot{R}$ because the term is derived from $2\mu\frac{\partial \dot{r}}{\partial r}\Big|_{r=R}$.

Finally, the Rayleigh–Plesset equation is derived by inserting Eq. (2.11) into Eq. (2.10).

$$R\ddot{R} + \frac{3}{2}\dot{R}^2 = \frac{1}{\rho_0}\left[p_g + p_v - \frac{2\sigma}{R} - \frac{4\mu\dot{R}}{R} - p_0 - p_s(t)\right] \tag{2.12}$$

where p_0 is the ambient static pressure, and $p_s(t)$ is the instantaneous acoustic pressure at time t ($p_\infty = p_0 + p_s(t)$). As the incompressibility of the liquid is assumed in the derivation of Eq. (2.12), the equation is no longer valid when a bubble violently collapses with speed comparable to sound velocity in the liquid.

2.2 Rayleigh Collapse

After bubble expansion during the rarefaction phase of ultrasound, a bubble violently collapses if the ambient bubble radius reaches a critical range. The range of ambient radius for an active bubble is discussed in Sect. 2.12. In this section, the cause for the violent collapse of a bubble is discussed using the Rayleigh–Plesset equation [2]. From Eq. (2.12), the bubble wall acceleration ($\ddot{R}$) is expressed as follows.

$$\ddot{R} = -\frac{3\dot{R}^2}{2R} + \frac{1}{\rho_0 R}\left[p_g + p_v - \frac{2\sigma}{R} - \frac{4\mu\dot{R}}{R} - p_0 - p_s(t)\right] \tag{2.13}$$

When a bubble violently collapses and $\dot{R}^2$ increases, the first term on right-hand side of Eq. (2.13) becomes dominant, and the second term becomes negligible. In this situation, the following relationship nearly holds.

$$\ddot{R} \approx -\frac{3\dot{R}^2}{2R} \tag{2.14}$$

This means that the bubble wall acceleration ($\ddot{R}$) is always negative. It results in a decrease in the bubble wall velocity ($\dot{R}$). As the bubble wall velocity is negative during the bubble collapse, the magnitude of bubble wall velocity increases with time. Then, the magnitude on the right-hand side of Eq. (2.14) further increases, and the magnitude of the bubble wall acceleration further increases. In this way, the bubble collapse freely accelerates, which is the reason for the violent bubble collapse called the *Rayleigh collapse*. Finally, the pressure (p_g) inside a bubble dramatically increases when the density inside a bubble becomes comparable to that of condensed phase (liquid). Then, the second term in Eq. (2.13) becomes dominant, and the bubble collapse stops as the bubble wall acceleration takes a large positive value.

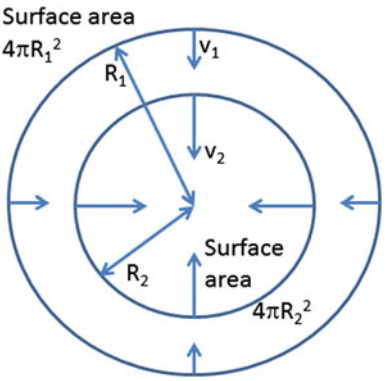

Fig. 2.3 Spherically inward flow as the mechanism for the violent collapse of a cavitation bubble. Reprinted with permission from Yasui [2]. Copyright (2015), Elsevier

The question that one may ask is: What is the physical reason for the freely accelerating collapse of a bubble? There are two reasons for it. One is the inertia of the surrounding liquid which flows toward a bubble during the bubble collapse. Thus, cavitation with such violent collapse of bubbles is called *inertial cavitation* (or *transient cavitation*). The other reason for the freely accelerating collapse is the geometry of a spherical collapse. Due to the conservation of mass, the velocity of the liquid toward the center of a bubble increases as the distance from the center of a bubble decreases. Let us consider two concentric spherical surfaces in a liquid with their center at the center of a bubble (Fig. 2.3) [2]. The radii of two concentric spherical surfaces are R_1 and R_2 $(R_1 > R_2)$. The mass (liquid) flow rate is $4\pi R_1^2 v_1$ and $4\pi R_2^2 v_2$ at the spherical surface of radii R_1 and R_2, respectively. The conservation of mass yields $4\pi R_1^2 v_1 = 4\pi R_2^2 v_2$. Thus, the velocity for smaller radius is larger, $v_2 = \left(\frac{R_1}{R_2}\right)^2 v_1 > v_1$. This is a nature of a spherical geometry which causes freely accelerating collapse of a bubble.

2.3 Keller Equation

The effect of liquid compressibility is approximately taken into account in bubble dynamics equation as follows: The starting equations are the continuity equation (conservation of mass) (Eq. 2.15) and Euler equation (equation of motion) (Eq. 2.16) [4–6].

$$\frac{\partial \rho}{\partial t} + \nabla \cdot (\rho \vec{u}) = \frac{\partial \rho}{\partial t} + \vec{u} \cdot \nabla \rho + \rho \nabla \cdot \vec{u} = 0 \tag{2.15}$$

$$\rho \frac{\mathrm{D}\vec{u}}{\mathrm{D}t} = \rho \left(\frac{\partial \vec{u}}{\partial t} + (\vec{u} \cdot \nabla)\vec{u} \right) = -\nabla p \tag{2.16}$$

where $\nabla = \left(\frac{\partial}{\partial x}, \frac{\partial}{\partial y}, \frac{\partial}{\partial z}\right)$, $\nabla \cdot (\rho \vec{u}) = \frac{\partial}{\partial x}(\rho u_x) + \frac{\partial}{\partial y}(\rho u_y) + \frac{\partial}{\partial z}(\rho u_z)$, ρ is the instantaneous local density of liquid, $\vec{u}$ is the instantaneous local velocity of liquid $\left(\vec{u} = (u_x, u_y, u_z)\right)$, $\nabla \rho = \left(\frac{\partial \rho}{\partial x}, \frac{\partial \rho}{\partial y}, \frac{\partial \rho}{\partial z}\right)$, $\frac{\mathrm{D}}{\mathrm{D}t}$ is the material time derivative $\left(\frac{\mathrm{D}}{\mathrm{D}t} = \frac{\partial}{\partial t} + \vec{u} \cdot \nabla\right)$, $\vec{u} \cdot \nabla = u_x \frac{\partial}{\partial x} + u_y \frac{\partial}{\partial y} + u_z \frac{\partial}{\partial z}$, and p is the instantaneous local pressure of the liquid. In Eq. (2.16), the effects of gravitational force and liquid viscosity are neglected. The derivation of the above equations is described in detail in textbooks of fluid dynamics [7].

Here, it is assumed that the velocity field of the liquid around a pulsating bubble has only a radial component. In this case, the liquid flow is irrotational, and the velocity field is expressed by using a velocity potential (ϕ).

$$\vec{u} = \nabla \phi = \frac{\partial \phi}{\partial r} \overrightarrow{e_{\mathrm{r}}} \tag{2.17}$$

where r is radial distance from the center of a bubble, and $\overrightarrow{e_{\mathrm{r}}}$ is a radial unit vector. Then, Eqs. (2.15) and (2.16) are expressed as Eqs. (2.18) and (2.19), respectively.

$$\frac{\partial \rho}{\partial t} + \left(\frac{\partial \phi}{\partial r}\right)\left(\frac{\partial \rho}{\partial r}\right) + \rho \Delta \phi = 0 \tag{2.18}$$

$$\rho \left[\frac{\partial^2 \phi}{\partial t \partial r} + \left(\frac{\partial \phi}{\partial r}\right)\left(\frac{\partial^2 \phi}{\partial r^2}\right)\right] = -\frac{\partial p}{\partial r} \tag{2.19}$$

From Eqs. (2.18) and (2.19), the following modified wave equation is derived (for a detailed method of derivation, see Ref. [4]).

$$\Delta \phi - \frac{1}{c^2}\frac{\partial^2 \phi}{\partial t^2} = \frac{1}{c^2}\left(\frac{\partial \phi}{\partial r}\right)\left(\frac{\partial^2 \phi}{\partial r \partial t}\right) - \frac{1}{\rho}\left(\frac{\partial \rho}{\partial r}\right)\left(\frac{\partial \phi}{\partial r}\right) \tag{2.20}$$

where c is the instantaneous local sound velocity. In the derivation of the Keller equation of bubble dynamics, the right-hand side of Eq. (2.20) is neglected and the wave equation (Eq. 2.21) can be used. Thus, the Keller equation is an approximate equation which is only valid when $\frac{|\dot{R}|}{c_\infty} \ll 1$, where c_∞ is the sound velocity at ambient condition.

$$\Delta \phi - \frac{1}{c_\infty^2}\frac{\partial^2 \phi}{\partial t^2} = 0 \tag{2.21}$$

By integrating Eq. (2.19) with respect to r, the following approximate equation may be derived [4].

$$\frac{\partial \phi}{\partial t} + \frac{1}{2}u^2 + \frac{p - p_\infty}{\rho_{\mathrm{L},\infty}} = 0 \tag{2.22}$$

where p_∞ is the ambient pressure, and the liquid density is assumed constant at ambient conditions $\left(\rho = \rho_{\mathrm{L},\infty} = \text{const.}\right)$. The boundary condition is given as follows.

$$\left(\frac{\partial \phi}{\partial r}\right)_{r=R} = \dot{R} \tag{2.23}$$

The general solution of the wave equation (Eq. 2.21) under spherical symmetry is given as follows.

$$\phi = -\frac{f\left(t - \frac{r}{c_\infty}\right)}{r} - \frac{g\left(t + \frac{r}{c_\infty}\right)}{r} \tag{2.24}$$

where f and g are arbitrary functions. From Eqs. (2.23) and (2.24), Eq. (2.25) is obtained.

$$\frac{f'}{R} = c_\infty \left[\dot{R} + \frac{\phi(R)}{R}\right] + \frac{g'}{R} \tag{2.25}$$

where $'$ means derivative. From Eqs. (2.24) and (2.25), Eq. (2.26) is obtained.

$$\left(\frac{\partial \phi}{\partial t}\right)_{r=R} = -c_\infty \left[\dot{R} + \frac{\phi(R)}{R}\right] - \frac{2g'}{R} \tag{2.26}$$

Inserting Eqs. (2.23) and (2.26) into Eq. (2.22) yields Eq. (2.27).

$$-c_\infty \left[\dot{R} + \frac{\phi(R)}{R}\right] - \frac{2g'}{R} + \frac{1}{2}\dot{R}^2 + \frac{p_\mathrm{B} - p_\infty}{\rho_{\mathrm{L},\infty}} = 0 \tag{2.27}$$

where p_B is the liquid pressure at the bubble. Thus, multiplying Eq. (2.27) by R and differentiating by t yields Eq. (2.28).

$$\begin{aligned} 0 = &-c_\infty \left[\dot{R}^2 + R\ddot{R} + \left(\frac{\mathrm{d}\phi}{\mathrm{d}t}\right)_{r=R}\right] \\ &- 2\frac{\mathrm{d}g'}{\mathrm{d}t} + \frac{1}{2}\dot{R}^3 + R\dot{R}\ddot{R} + \frac{R}{\rho_{\mathrm{L},\infty}}\frac{\mathrm{d}p_\mathrm{B}}{\mathrm{d}t} + \frac{1}{\rho_{\mathrm{L},\infty}}\dot{R}(p_\mathrm{B} - p_\infty) \end{aligned} \tag{2.28}$$

where $''$ means the second derivative. From Eqs. (2.22) and (2.23), Eq. (2.29) is obtained.

$$\left(\frac{\mathrm{d}\phi}{\mathrm{d}t}\right)_{r=R} = \frac{\partial\phi}{\partial t} + \frac{\partial\phi}{\partial r}\frac{\mathrm{d}r}{\mathrm{d}t} = -\frac{1}{2}\dot{R}^2 - \frac{p_\mathrm{B} - p_\infty}{\rho_{\mathrm{L},\infty}} + \dot{R}^2 \tag{2.29}$$

When the incident field is a plane acoustic wave with an angular frequency ω and a pressure amplitude A, the following relationship holds [4].

$$2g'' = -\frac{c_\infty}{\rho_{\mathrm{L},\infty}} A \sin\omega t \tag{2.30}$$

Inserting Eqs. (2.29) and (2.30) into Eq. (2.28) yields the equation of bubble dynamics called the Keller equation (Eq. 2.31).

$$\left(1 - \frac{\dot{R}}{c_\infty}\right)R\ddot{R} + \frac{3}{2}\dot{R}^2\left(1 - \frac{\dot{R}}{3c_\infty}\right) = \frac{1}{\rho_{\mathrm{L},\infty}}\left(1 + \frac{\dot{R}}{c_\infty}\right)[p_\mathrm{B} - p_\mathrm{s}(t) - p_\infty] + \frac{R}{c_\infty\rho_{\mathrm{L},\infty}}\frac{\mathrm{d}p_B}{\mathrm{d}t} \tag{2.31}$$

where $A \sin\omega t$ is replaced by $p_\mathrm{s}(t)$.

As already noted, the Keller equation is valid only when $\frac{|\dot{R}|}{c_\infty} \ll 1$. However, in numerical simulations using the Keller equation, this condition is often violated during a violent bubble collapse. When $|\dot{R}|$ exceeds c_∞, $\left(1 + \frac{\dot{R}}{c_\infty}\right)$ in the right-hand side of Eq. (2.31) changes sign, and the error in numerical calculations becomes significant. To avoid this error, c_∞ in Eq. (2.31) is sometimes replaced by the sound velocity in the liquid at the bubble wall $(c_{\mathrm{L,B}})$. It dramatically increases as the liquid pressure at the bubble wall increases as follows [8, 9].

$$c_{\mathrm{L,B}} = \sqrt{\frac{7.15(p_\mathrm{B} + B)}{\rho_{\mathrm{L,i}}}} \tag{2.32}$$

where $c_{\mathrm{L,B}}$ is the sound velocity in the liquid water at the bubble wall, $B = 3.049 \times 10^8$ (Pa), and $\rho_{\mathrm{L,i}}$ is the liquid density at the bubble wall. The liquid density at the bubble wall is a function of pressure and temperature at the bubble wall [6]. In numerical simulations using the Keller equation, the bubble wall speed $|\dot{R}|$ sometimes still exceeds $c_{\mathrm{L,B}}$. In that case, the bubble wall speed is replaced by $c_{\mathrm{L,B}}$ because the bubble wall speed never exceeds $c_{\mathrm{L,B}}$ according to the following arguments [9].

For steady flows $\left(\frac{\partial\vec{u}}{\partial t} = 0\right)$, the Euler equation (Eq. 2.16) yields Eq. (2.33) [10].

$$u\mathrm{d}u = -\frac{\mathrm{d}p}{\rho} = -\frac{\mathrm{d}p}{\mathrm{d}\rho}\frac{\mathrm{d}\rho}{\rho} = -c^2\frac{\mathrm{d}\rho}{\rho} \tag{2.33}$$

where the following relationship for sound velocity is used.

$$c = \sqrt{\frac{\mathrm{d}p}{\mathrm{d}\rho}} \tag{2.34}$$

Using Mach number $M = \frac{u}{c}$, Eq. (2.33) becomes Eq. (2.35).

$$\frac{\mathrm{d}\rho}{\rho} = -M^2 \frac{\mathrm{d}u}{u} \tag{2.35}$$

For radial steady flows $\left(\frac{\partial \rho}{\partial t} = 0\right)$ toward the center of a bubble, the conservation of mass requires the following relationship [10].

$$\rho u A_\mathrm{s} = \text{independent of } r \tag{2.36}$$

where A_s is the surface area of a sphere $(A_\mathrm{s} = 4\pi r^2)$. The differentiation of Eq. (2.36) yields Eq. (2.37).

$$uA_\mathrm{s} \cdot \mathrm{d}\rho + \rho A_\mathrm{s} \cdot \mathrm{d}u + \rho u \cdot \mathrm{d}A_\mathrm{s} = 0 \tag{2.37}$$

Equation (2.37) is equivalent to the following equation.

$$\frac{\mathrm{d}\rho}{\rho} + \frac{\mathrm{d}u}{u} + \frac{\mathrm{d}A_\mathrm{s}}{A_\mathrm{s}} = 0 \tag{2.38}$$

Inserting Eq. (2.35) into Eq. (2.38) yields Eq. (2.39).

$$\frac{\mathrm{d}u}{u} = -\frac{\frac{\mathrm{d}A_\mathrm{s}}{A_\mathrm{s}}}{(1 - M^2)} = -\frac{2\mathrm{d}r/r}{(1 - M^2)} \tag{2.39}$$

where $A_\mathrm{s} = 4\pi r^2$ is used. As already discussed in Sect. 2.2, the magnitude of the liquid velocity increases (the liquid velocity decreases because $u < 0$ for inward liquid flow) as the radial distance from the center of the bubble decreases ($\mathrm{d}u < 0$ for $\mathrm{d}r < 0$). From Eq. (2.39), it implies that $|M| < 1$.

In the above discussion, a liquid flow is assumed as steady ($\frac{\partial u}{\partial t} = 0$ and $\frac{\partial \rho}{\partial t} = 0$). Under typical conditions of a bubble collapse, the terms $\frac{\partial u}{\partial t}$ and $\frac{\partial \rho}{\partial t}$ are actually negligible compared to the other terms in the Euler equation and the equation of continuity, respectively. However, further studies are required on the upper limit of the bubble wall speed in the case of non-steady flows. Furthermore, the method of numerical simulations of the Keller equation discussed above is rather "tricky." Rigorous derivation of more accurate equation of the bubble dynamics is an important focus and task. Of relevance, there have been a few studies based upon the direct numerical simulations of the bubble collapse employing fundamental equations of fluid dynamics [11, 12].

2.4 Method of Numerical Simulations

For quantitative discussions on bubble pulsation, numerical simulations of the Keller equation and other equations of bubble dynamics are required. The simplest method of numerical simulation is the Euler method [2, 13].

$$R(t+\Delta t) = R(t) + \dot{R}(t)\Delta t \tag{2.40}$$

where $R(t)$ is the instantaneous bubble radius at time t, Δt is a time step in numerical simulation. In numerical simulations, the continuous time is divided into a large number of discrete times with a small unit step (Δt). Equation (2.40) is derived directly from the definition of the time derivative.

$$\dot{R}(t) = \lim_{\Delta t \to 0} \frac{R(t+\Delta t) - R(t)}{\Delta t} \tag{2.41}$$

The bubble wall velocity $(\dot{R})$ is also calculated in the same manner.

$$\dot{R}(t+\Delta t) = \dot{R}(t) + \ddot{R}(t)\Delta t \tag{2.42}$$

The bubble wall acceleration $\left(\ddot{R}(t)\right)$ is calculated by the Keller equation (Eq. 2.31) and other equations of bubble dynamics. For numerical simulations, initial values of R and $\dot{R}$ are required. When the Keller equation is used, initial values of p_{B} and $\frac{\mathrm{d}p_B}{\mathrm{d}t}$ are also required. At an arbitrary time, the pressure inside a bubble $(p_{\mathrm{in}} = p_{\mathrm{g}} + p_{\mathrm{v}})$ needs to be calculated in order to calculate p_{B} and $\ddot{R}(t)$. For this purpose, the van der Waals equation of state is used [14].

$$\left[p_{\mathrm{in}} + \frac{a_v}{v^2}\right](v - b_v) = R_g T \tag{2.43}$$

where a_v and b_v are the van der Waals constants, v is the molar volume, R_g is the gas constant, and T is the temperature inside a bubble. The molar volume v is calculated as follows.

$$v = \frac{4\pi R^3}{3} \cdot \frac{\mathrm{N_A}}{n_{\mathrm{t}}} \tag{2.44}$$

where $\mathrm{N_A}$ is the Avogadro number ($= 6.02 \times 10^{23}$ mol^{-1}), and n_{t} is the total number of molecules inside a bubble. In order to calculate the pressure inside a bubble (p_{in}), the temperature and the total number of molecules inside a bubble are required. The temperature (T) inside a bubble is approximately calculated from internal thermal energy (E) of a bubble as follows [14].

$$E = \frac{T}{\mathrm{N_A}} \sum_{\alpha} n_\alpha C_{\mathrm{V},\alpha} - \left(\frac{n_\mathrm{t}}{\mathrm{N_A}}\right)^2 \frac{a_v}{V} \tag{2.45}$$

where n_α is the number of molecules of species α inside a bubble, $C_{\mathrm{V},\alpha}$ is the molar heat capacity at constant volume of species α, the summation is for all the gas and vapor species inside a bubble, and V is the bubble volume $\left(V = \frac{4}{3}\pi R^3\right)$. The derivation of Eq. (2.45) is as follows [15, 16]. The internal energy (E) of a bubble is a function of temperature (T) and volume (V) of a bubble for the van der Waals gas.

$$\mathrm{d}E = \left(\frac{\partial E}{\partial T}\right)_V \mathrm{d}T + \left(\frac{\partial E}{\partial V}\right)_T \mathrm{d}V \tag{2.46}$$

From the definition of the molar heat capacity at constant volume, the following relationship holds.

$$\left(\frac{\partial E}{\partial T}\right)_V = \frac{1}{\mathrm{N_A}} \sum_{\alpha} n_\alpha C_{\mathrm{V},\alpha} \tag{2.47}$$

For the van der Waals gas, the second term on the right-hand side of Eq. (2.46) is nonzero.

$$\left(\frac{\partial E}{\partial V}\right)_T = T\left(\frac{\partial p_\mathrm{in}}{\partial T}\right)_V - p_\mathrm{in} = \left(\frac{n_\mathrm{t}}{\mathrm{N_A}}\right)^2 \frac{a_v}{V^2} \tag{2.48}$$

Using Eqs. (2.47) and (2.48), integration of Eq. (2.46) yields Eq. (2.45) assuming temperature-independent molar heat at constant volume. The temporal change in the total number (n_t) of molecules as well as those of species α inside a bubble is discussed in Sects. 2.5–2.9.

The temporal change (ΔE) in an internal thermal energy of a bubble is calculated as follows [14].

$$\begin{aligned}\Delta E = {} & -p_\mathrm{in}\Delta V + 4\pi R^2 \dot{m} e_{\mathrm{H_2O}} \Delta t + 4\pi R^2 \kappa \left.\frac{\partial T}{\partial r}\right|_{r=R} \Delta t + \frac{4}{3}\pi R^3 \Delta t \sum_r \left(r_{\gamma\mathrm{b}} - r_{\gamma\mathrm{f}}\right) \Delta H_{\gamma\mathrm{f}} \\ & + \sum_{\alpha'} e_{\alpha'} \Delta n_{\alpha'} + \left[-\frac{3}{5} M_\mathrm{in} \dot{R}\ddot{R}\right] \Delta t\end{aligned} \tag{2.49}$$

where $\dot{m}$ is the rate of non-equilibrium evaporation at the bubble wall, $e_{\mathrm{H_2O}}$ is the energy carried by an evaporating or condensing vapor molecule, κ is the thermal conductivity of a mixture of gases and vapor, $\left.\frac{\partial T}{\partial r}\right|_{r=R}$ is the temperature gradient

inside a bubble at the bubble wall, $r_{\gamma b}$ and $r_{\gamma f}$ are the backward and forward reaction rates, respectively, of chemical reaction γ per unit volume and unit time, $\Delta H_{\gamma f}$ is the enthalpy change in the forward reaction (when $\Delta H_{\gamma f} < 0$, i.e., the reaction is exothermic), the summation is for all the chemical reactions occurring inside a bubble, $e_{\alpha'}$ is the energy carried by a diffusing gas molecule of species α', $\Delta n_{\alpha'}$ is the change in number of molecules of species α' by diffusion, the summation is for all the gas species except vapor inside a bubble, and M_{in} is the total mass of gases and vapor inside a bubble. The first term on the right-hand side of Eq. (2.49) is the pV work done by the surrounding liquid on a bubble. The second term is the energy change associated with evaporation or condensation. The third term is the energy change due to the thermal conduction. The fourth term is the heat of chemical reactions. The fifth term is the energy change due to diffusion. The last term is included only when the quantity in the brackets is positive and is the heat due to the decrease in kinetic energy of gases and vapor inside a collapsing bubble. The derivation of the last term is given in Ref. [14]. More details of the model are described in Refs. [14, 17], and there are other similar models from various researchers [18, 19].

The results of numerical simulations based upon the present model of the bubble dynamics are shown in Figs. 2.4 and 2.5 under a condition of single-bubble sonoluminescence (SBSL) [2]. A bubble expands during the rarefaction phase of ultrasound (Fig. 2.4a). In order to make a bubble initially expand, $p_s(t)$ in Eq. (2.31) is assumed as $p_s(t) = -A \sin \omega t$. During the compression phase of ultrasound, a bubble violently collapses followed by bouncing motion (weaker

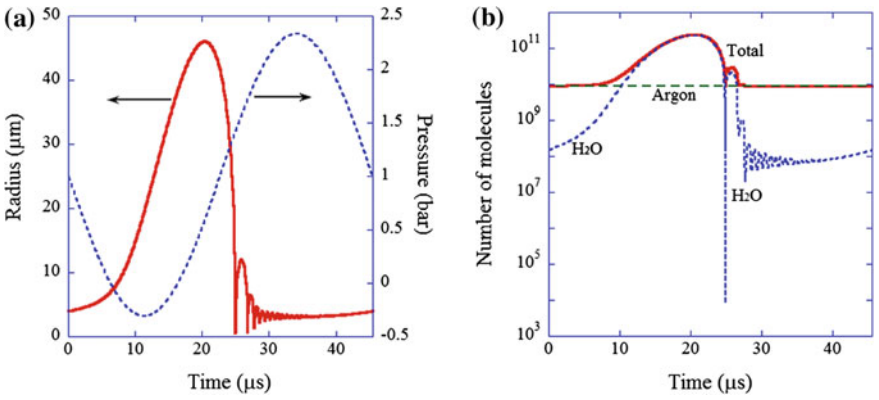

Fig. 2.4 Results of numerical simulations of bubble pulsation under a SBSL condition as a function of time for one acoustic cycle. The frequency and pressure amplitude of the acting ultrasound are 22 kHz and 1.32 bar, respectively. The ambient (equilibrium) bubble radius is 4 μm for an argon (Ar) bubble in 20 °C water. **a** The bubble radius (solid line) and the pressure $[p_\infty + p_s(t)]$ (dotted line) **b** The number of molecules inside a bubble on a logarithmic scale. Reprinted with permission from Yasui [2]. Copyright (2015), Elsevier

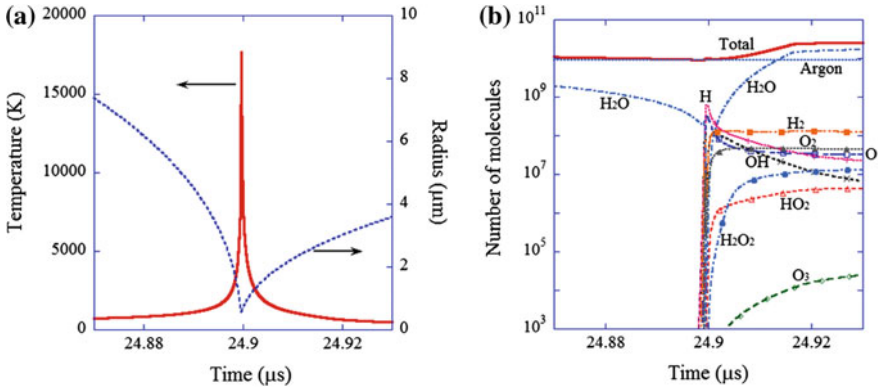

Fig. 2.5 Results of numerical simulations around the bubble collapse as a function of time, specifically for 0.06 μs (the condition is the same as that of Fig. 2.4). **a** The bubble radius (dotted line) and the temperature inside a bubble (solid line). **b** The number of molecules inside a bubble on a logarithmic scale. At $t = 24.93$ ms (the right end of the graph), the main chemical products are H_2 (1×10^8 in number of molecules), O_2 (4×10^7), O (3×10^7), H (2×10^7), H_2O_2 (1×10^7), and OH (7×10^6). Reprinted with permission from Yasui [2]. Copyright (2015), Elsevier

pulsation). During the bubble expansion, the number of H_2O molecules inside a bubble increases by evaporation at the bubble wall as the pressure inside a bubble decreases. During the bubble collapse, the number of H_2O molecules decreases by condensation at the bubble wall.

In the present numerical simulations, the non-condensable gas inside a bubble is assumed as argon (Ar). In SBSL, N_2 and O_2 in an air bubble chemically react due to the high temperature and pressure inside a bubble at each collapse of a bubble. As a result, soluble species such as HNO_x and NO_x are formed inside the bubble. These species gradually dissolve into the surrounding liquid water. Finally, chemically inactive species argon, which constitutes 1% of air, remains inside a SBSL bubble. This argon rectification hypothesis has been confirmed both experimentally and theoretically [20, 21]. Thus, in the present numerical simulations, an argon bubble is investigated.

According to the present numerical simulation, the temperature inside a bubble increases to 18,000 K at the end of the bubble collapse (Fig. 2.5a). The increase in temperature is mostly due to the pV work done by the surrounding liquid on a bubble. A bubble is substantially cooled by thermal conduction and endothermic chemical reactions. Thus, the bubble collapse is *quasi*-adiabatic. Due to the high temperature and pressure inside a bubble, almost all water vapor molecules trapped inside a bubble are dissociated, and hydrogen (H_2), oxygen (O_2), and hydroxyl radicals ($OH^\bullet$) are created (Fig. 2.5b). OH radicals play an important role in sonochemistry as previously discussed.

2.5 Non-equilibrium Evaporation and Condensation

There are two types of mass transfer across the bubble wall. One is non-equilibrium evaporation and condensation of (water) vapor at the bubble wall. The other is the diffusion of non-condensable gases across the bubble wall. In this section, non-equilibrium evaporation and condensation of water vapor is discussed. There are two steps in non-equilibrium evaporation and condensation processes (Fig. 2.6) [22]. One is the diffusion of water vapor inside a bubble. The other is the phase change at the bubble wall. According to full numerical simulations by Storey and Szeri [23], the diffusion of water vapor inside a bubble is sometimes the rate-determining step. According to their full numerical simulations [23], the molar fraction of water vapor near the bubble wall inside a bubble is about one order of magnitude smaller than that at the center of a bubble near the final stage of a violent bubble collapse. However, in their numerical simulations [23], fluid velocity inside a collapsing bubble is assumed to have only radial component. The possible appearance of non-radial component of fluid velocity inside a collapsing bubble such as in turbulence should be studied in future. If turbulence occurs inside a collapsing bubble, molar fraction of water vapor is more homogeneous.

There is another issue on inhomogeneous molar fraction of water vapor inside a collapsing bubble. According to numerical simulations by Storey and Szeri [8], there are intense temperature and pressure gradients inside a collapsing bubble. These gradients drive relative mass diffusion which overwhelms diffusion driven by concentration gradients. These thermal and pressure diffusion processes result in a robust compositional inhomogeneity in the bubble which lasts for several orders of magnitude longer than the temperature peak. In their study on the mixture segregation [8], a mixture of He and Ar gases was investigated. Mixture segregation occurs for a mixture of gases with large difference in their molecular weights. When molecular weight of non-condensable gas is largely different from that of water vapor, water vapor and non-condensable gas are expected to be mildly segregated inside a collapsing bubble [8, 24, 25]. In this case, rate of non-equilibrium condensation during bubble collapse is strongly influenced by mixture segregation. Further studies are required on whether mixture segregation occurs inside a collapsing bubble.

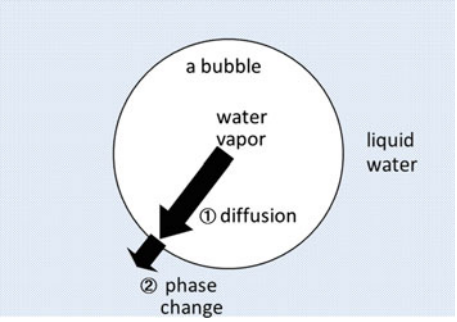

Fig. 2.6 Two steps in vapor transport inside a bubble to the bubble wall. Reprinted with permission from Yasui et al. [22]. Copyright (2004), Taylor & Francis

If the rate-determining step is the phase change, the rate $(\dot{m})$ of non-equilibrium evaporation and condensation at the bubble wall is given by the following equations [14, 26, 27].

$$\dot{m} = \dot{m}_{\mathrm{eva}} - \dot{m}_{\mathrm{con}} \tag{2.50}$$

$$\dot{m}_{\mathrm{eva}} = \frac{10^3 \mathrm{N_A}}{M_{\mathrm{H_2O}}} \frac{\alpha_{\mathrm{M}}}{\sqrt{2\pi R_v}} \frac{p_{\mathrm{v}}^*}{\sqrt{T_{\mathrm{L,i}}}} \tag{2.51}$$

$$\dot{m}_{\mathrm{con}} = \frac{10^3 \mathrm{N_A}}{M_{\mathrm{H_2O}}} \frac{\alpha_{\mathrm{M}}}{\sqrt{2\pi R_{\mathrm{v}}}} \frac{\Gamma p_{\mathrm{v}}}{\sqrt{T_{\mathrm{B}}}} \tag{2.52}$$

where $\dot{m}_{\mathrm{eva}}$ and $\dot{m}_{\mathrm{con}}$ are actual rates of evaporation and condensation ($\dot{m}$ is the net rate of evaporation), $M_{\mathrm{H_2O}}$ is the molecular weight of H_2O (=18 g/mol), and α_{M} is the accommodation coefficient for evaporation or condensation. R_{v} is the gas constant of water vapor in (J/kg K), p_{v}^* is the saturated vapor pressure at the liquid temperature $(T_{\mathrm{L,i}})$ at the bubble wall, p_{v} is actual vapor pressure inside a bubble, T_{B} is the temperature at the bubble wall inside a bubble, and the correction factor (Γ) is given as follows.

$$\Gamma = \mathrm{e}^{-\Omega^2} - \Omega\sqrt{\pi}\left(1 - \frac{2}{\sqrt{\pi}} \int_0^{\Omega} \mathrm{e}^{-x^2} \mathrm{d}x\right) \tag{2.53}$$

where

$$\Omega = \frac{\dot{m}}{p_{\mathrm{v}}} \left(\frac{R_{\mathrm{v}} T}{2}\right)^{1/2} \tag{2.54}$$

The actual vapor pressure (p_{v}) inside a bubble is given as follows.

$$p_{\mathrm{v}} = \frac{n_{\mathrm{H_2O}}}{n_{\mathrm{t}}} p_{\mathrm{in}} \tag{2.55}$$

where $n_{\mathrm{H_2O}}$ is the number of H_2O molecules inside a bubble. Equations (2.50)–(2.52) are derived assuming a thin boundary layer near the liquid–gas interface in which the velocity distribution of molecules is Maxwell–Boltzmann [26]. From the velocity distribution, the collision frequency of molecules at the surface of a boundary layer is calculated. By multiplying it with the accommodation coefficient which is a probability of escaping the boundary layer for a molecule, the actual rates of evaporation and condensation are obtained. The accommodation coefficient is a function of the liquid temperature at the bubble wall: It decreases from 0.35 at 350 K to 0.05 at 500 K according to the molecular dynamics simulations by Matsumoto [14, 28].

According to numerical simulations, the non-equilibrium effect is only dominant at a bubble collapse [29]. At a strong collapse, the vapor pressure (p_v) inside a bubble is higher than the saturated vapor pressure (p_v^*) at the liquid temperature at the bubble wall $(T_{L,i})$ by more than one order of magnitude. On the other hand, during the bubble expansion, the vapor pressure is nearly identical to the saturated vapor pressure (nearly in equilibrium).

When diffusion is sometimes rate-determining step, the reader should refer to Refs. [18, 19].

2.6 Liquid Temperature at the Bubble Wall

Another important problem is the liquid temperature at the bubble wall. In numerical simulations, it is sometimes assumed to be identical to the ambient liquid temperature [18, 19]. However, there are some experimental evidences on the substantial increase in liquid temperature at the bubble wall [30–32]. For example, Suslick et al. [30] experimentally studied reaction rates of metal carbonyls in alkane solvent as a function of solvent vapor pressure when solutions were irradiated with ultrasound at 20 kHz. From the vapor pressure-independent component, they estimated the temperature at the interface between a bubble and liquid as $\sim$1900 K. Hua et al. [31] experimentally studied sonochemical degradation of nonvolatile hydrophobic *p*-nitrophenyl acetate and concluded that the degradation was accelerated by supercritical water formed at the bubble interface region (Fig. 2.7) [33]. Supercritical water is defined as water at temperature and pressure higher than the critical ones (647 K and 221 bar, respectively). Moriwaki et al. [32] experimentally studied the sonochemical degradation of anionic surfactants and concluded that they were pyrolyzed at the interfacial region of a bubble. Thus, for accurate numerical simulations, the increase in temperature at the interface region of a bubble should be taken into account. There are some models available to determine the liquid temperature $(T_{L,i})$ at the bubble wall [6, 8, 34–36]. According

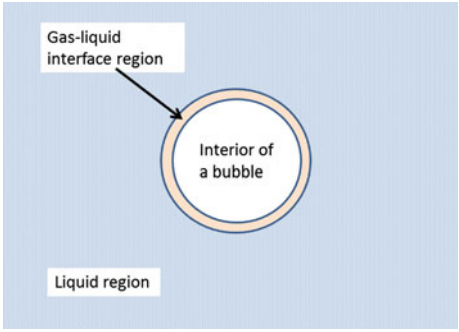

Fig. 2.7 Three regions for a cavitation bubble. Reprinted with permission from Yasui [33]. Copyright (2016), Springer

to the full numerical simulations by Storey and Szeri [23], the temperature of the interface exceeds the critical point (647 K) for about 2 ns at around the minimum bubble radius. The thickness of supercritical region is only about 10 nm. More studies are required to further elucidate the interface temperature at the bubble collapse.

2.7 Gas Diffusion (Rectified Diffusion)

Gas diffusion across the bubble surface is a complex phenomenon when a bubble is pulsating under ultrasound because the gas concentration in the liquid adjacent to bubble wall changes in an intricate way. Eller and Flynn [37] solved this problem in 1965 using material coordinates, which move as the liquid element moves. They solved the diffusion equation for a pulsating bubble by time averaging over an acoustic period as follows [37].

$$\left\langle \frac{\mathrm{d}n_{\mathrm{gas}}}{\mathrm{d}t} \right\rangle = 4\pi R_0 D_{\mathrm{gas}} \left[A_{\mathrm{R}} + R_0 \left(\frac{B_{\mathrm{R}}}{\pi D_{\mathrm{gas}} t} \right)^{1/2} \right] c_{\mathrm{i}0} \left(\frac{c_\infty}{c_{\mathrm{i}0}} - \frac{A_{\mathrm{R}}}{B_{\mathrm{R}}} \right) \tag{2.56}$$

where n_{gas} is the number of molecules of non-condensable gas inside a bubble, $\langle\ \rangle$ means time-averaged value, R_0 is the ambient bubble radius, D_{gas} is the diffusion coefficient of the gas in the liquid, $c_{\mathrm{i}0}$ is the gas concentration at the bubble wall in the liquid at ambient bubble radius (R_0), c_∞ is the ambient gas concentration in the liquid, and A_{R} and B_{R} is defined as follows.

$$A_{\mathrm{R}} = \frac{1}{T_{\mathrm{a}}} \int_0^{T_{\mathrm{a}}} \left(\frac{R}{R_0} \right) \mathrm{d}t \tag{2.57}$$

$$B_{\mathrm{R}} = \frac{1}{T_{\mathrm{a}}} \int_0^{T_{\mathrm{a}}} \left(\frac{R}{R_0} \right)^4 \mathrm{d}t \tag{2.58}$$

The gas concentration $(c_{\mathrm{i}0})$ at the bubble wall in the liquid at ambient bubble radius (R_0) is given by the following equation.

$$c_{\mathrm{i}0} = c_\infty \frac{p_{\mathrm{gas},0}}{p_\infty} \approx c_\infty \left(1 + \frac{2\sigma}{R_0 p_\infty} \right) \tag{2.59}$$

where $p_{\mathrm{gas},0}$ is pressure of gas inside a bubble at ambient bubble radius.

From the time-averaged rate of gas diffusion in Eq. (2.56), the instantaneous rate of gas diffusion is postulated in Ref. [38] as follows.

$$\frac{\mathrm{d}n_{\mathrm{gas}}}{\mathrm{d}t} = 4\pi R^2 D_{\mathrm{gas}} \frac{A_{\mathrm{R}}}{B_{\mathrm{R}}} \frac{c_\infty - c_{\mathrm{i}}}{(R_0/R)^2 R_0} \tag{2.60}$$

where c_{i} is the instantaneous gas concentration at the bubble wall in the liquid. In the derivation of Eq. (2.60) from Eq. (2.56), the second term in the square brackets in Eq. (2.56) is omitted, and the bubble pulsation is assumed to be isothermal as follows.

$$c_{\mathrm{i}} = c_\infty \frac{p_{\mathrm{gas}}}{p_\infty} \approx c_\infty \left(1 + \frac{2\sigma}{R_0 p_\infty}\right) \left(\frac{R_0}{R}\right)^3 \tag{2.61}$$

where p_{gas} is the instantaneous gas pressure inside a bubble, and $p_{\mathrm{gas}}\left(\frac{4}{3}\pi R^3\right) = p_{\mathrm{gas},0}\left(\frac{4}{3}\pi R_0^3\right)$ is used. This assumption is justified as the bubble expansion is nearly isothermal and gas diffusion occurs mostly during bubble expansion.

Gas diffuses into a bubble during bubble expansion as the pressure inside a bubble is lower than the ambient pressure [$c_\infty > c_{\mathrm{i}}$ in Eq. (2.60)]. During bubble collapse, the gas diffuses out of a bubble into surrounding liquid as the pressure inside a bubble is higher than the ambient pressure [$c_\infty < c_{\mathrm{i}}$ in Eq. (2.60)]. When a bubble is strongly pulsating, the gas diffusion into a bubble during the bubble expansion overwhelms that out of a bubble during the bubble collapse; this process is called *rectified diffusion* [39, 40]. There are two main reasons in rectified diffusion. One is the larger surface area during the bubble expansion than that during the bubble collapse; this is called *area effect*. The other is larger magnitude of gradient of gas concentration during the bubble expansion than that during the bubble collapse. This is due to thinner material (liquid) element during the bubble expansion compared to that during the bubble collapse; this is called *shell effect* (Fig. 2.8). In Eq. (2.60), the shell effect is expressed by $\left(\frac{R_0}{R}\right)^2$ in the denominator. The area effect is expressed by $4\pi R^2$ in Eq. (2.60).

Growth rate of a pulsating bubble by rectified diffusion is defined as the rate of increase in ambient bubble radius. The growth rate by rectified diffusion strongly

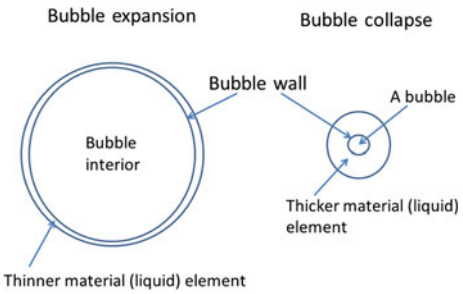

Fig. 2.8 Shell effect in rectified diffusion

depends upon the operating conditions, such as the acoustic pressure amplitude and the acoustic frequency as well as the surface tension. The growth rate of a bubble with an initial radius of 35 μm was experimentally measured as a few micrometers per 100 s when the ultrasonic frequency and pressure amplitude were 22.1 kHz and 0.3 bar, respectively, in air-saturated water [41]. At acoustic pressure amplitude of 2 bar at 26.5 kHz, growth rate by rectified diffusion is numerically calculated to range from 10 to several 100 μm/s depending upon the initial ambient radius in nearly gas-saturated water [42].

2.8 Chemical Kinetic Model

Generally speaking, chemical reactions inside a collapsing bubble are in non-equilibrium [43]. Thus, it is necessary to use chemical kinetic model for numerical simulations of chemical reactions inside a bubble. For example, the rate of the following reaction is given by Eq. (2.63) [14, 35].

$$\mathrm{H_2O} + M \rightarrow \mathrm{H} + \mathrm{OH} + M \tag{2.62}$$

$$r_\mathrm{f} = \mathrm{A_f} T^{\mathrm{b_f}} \mathrm{e}^{-\mathrm{C_f}/T} [\mathrm{H_2O}][M] \tag{2.63}$$

where $\mathrm{A_f}$, $\mathrm{b_f}$, and $\mathrm{C_f}$ are the rate constants of the reaction; T is the temperature inside a bubble; $[\mathrm{H_2O}]$ is the concentration of $\mathrm{H_2O}$ molecules inside a bubble; and $[M]$ is the concentration of any molecules (third body) inside a bubble. The subscript f denotes forward reaction. The rate constants of the chemical reactions inside a bubble are listed in Refs. [14, 17, 35, 44, 45].

Rate of the backward reaction of (2.62) can be calculated in a similar manner.

$$r_\mathrm{b} = \mathrm{A_b} T^{\mathrm{b_b}} \mathrm{e}^{-\mathrm{C_b}/T} [\mathrm{H}][\mathrm{OH}][M] \tag{2.64}$$

where $\mathrm{A_b}$, $\mathrm{b_b}$, and $\mathrm{C_b}$ are the rate constants of the backward reaction, and [H] and [OH] are concentrations of H and OH molecules inside a bubble, respectively. The subscript b denotes backward reaction. The rate constants for the backward reactions are also listed in Refs. [14, 17, 35, 44, 45].

2.9 Single-Bubble Sonochemistry

It is possible to validate a model for bubble dynamics by comparing it with the experimental results on single-bubble sonochemistry [46]. Experimental setup is similar to that of single-bubble sonoluminescence (Fig. 2.9) [22]. A stable single bubble is under controlled acoustic pressure and frequency as well as under controlled liquid temperature. Thus, it is possible to directly compare results of

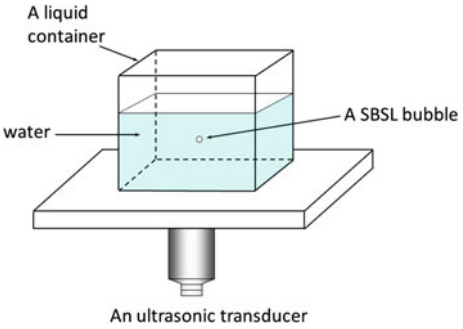

Fig. 2.9 Experimental setup for single-bubble sonochemistry or sonoluminescence (SBSL). Reprinted with permission from Yasui et al. [22]. Copyright (2004), Taylor & Francis

numerical simulation with the experimental data. In this system, there is no complexity due to other bubbles such as bubble–bubble interaction (Sect. 2.18).

In 2002, Didenko and Suslick [46] first reported quantitative results on single-bubble sonochemistry. They measured production rate of OH radicals from a single stable bubble using terephthalate dosimetry (as 8.2×10^5 molecules per acoustic cycle). The ultrasonic frequency and pressure amplitude were 52 kHz and 1.5 atm (=1.52 bar), respectively. The liquid temperature was 3 °C, and the maximum bubble radius was measured as 30.5 μm. The rate of NO_2^- ion production was measured as 9.9×10^6 ions per acoustic cycle, and the number of photons emitted in sonoluminescence was measured as 7.5×10^4.

Next, results of numerical simulation under the experimental condition of Didenko and Suslick [46] are briefly reviewed [17]. To produce the experimentally observed maximum radius of 30.5 μm, the ambient bubble radius was determined as $R_0 = 3.6\,\mu\text{m}$ (Fig. 2.10a) [17]. The dissolution of OH radicals into surrounding liquid was also numerically simulated by using uptake coefficient Θ defined as follows.

$$\Theta = \frac{N_{\text{in}} - N_{\text{out}}}{N_{\text{col}}} \tag{2.65}$$

where N_{in} is the number of molecules dissolving into the liquid, N_{out} is the number of molecules desorbing from the liquid into the gas, and N_{col} is the number of molecules colliding with the interface between gas and liquid. In the simulation in Ref. [17], the uptake coefficient was assumed to be $\Theta = 0.001$. The rate $(r_{\text{d,OH}})$ of dissolution of OH radicals into the liquid water from the interior of a bubble was calculated as follows.

$$r_{\text{d,OH}} = \Theta \sqrt{\frac{\text{k}T_{\text{B}}}{2\pi m_{\text{OH}}}} \frac{n_{\text{OH}}}{V} \times 4\pi R^2 \tag{2.66}$$

where k is Boltzmann constant (=1.38×10^{-23} J/K), T_{B} is the temperature at the bubble wall inside a bubble, m_{OH} is the molecular mass of OH radical (=2.82×10^{-26} kg), n_{OH} is the number of OH radicals inside a bubble, and V is the

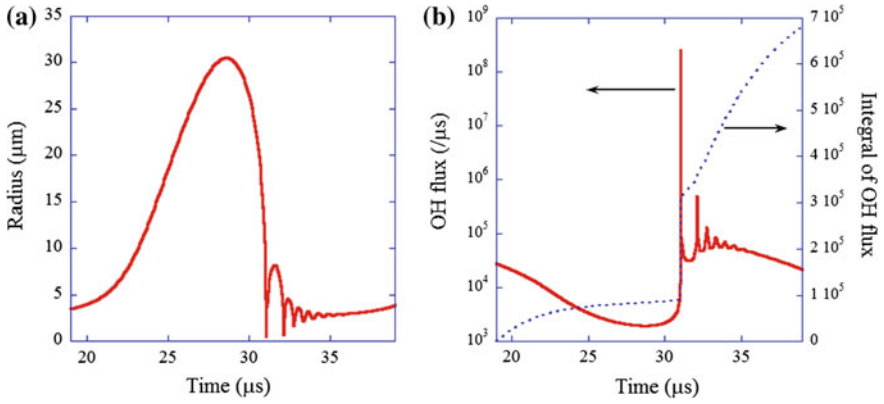

Fig. 2.10 Calculated results for one acoustic cycle when a SBSL bubble in a steady state in water at 3 °C is irradiated by an ultrasonic wave of 52 kHz and 1.52 bar in frequency and pressure amplitude, respectively. The ambient bubble radius is 3.6 μm. **a** The bubble radius. **b** The dissolution rate of OH radicals into the liquid from the interior of the bubble (solid line) and its time integral (dotted line). Reprinted with permission from Yasui et al. [17]. Copyright (2005), AIP Publishing LLC

volume of a bubble ($= \frac{4}{3}\pi R^3$). Equation (2.66) is the frequency of collision of OH radicals on the bubble surface multiplied by surface area of a bubble and uptake coefficient.

The result of numerical simulations on OH flux ($r_{\mathrm{d,OH}}$) is shown in Fig. 2.10b as a function of time for one acoustic cycle. The dotted line shows the time integral of the OH flux. The amount of OH radicals dissolved into the surrounding liquid from the interior of a bubble is calculated as 6.6×10^5 (number of molecules). It roughly agrees with the experimental data of 8.2×10^5. This finding means that the model of bubble dynamics including chemical kinetic model is almost validated.

The temperature inside a bubble increases up to 10,900 K at the end of the bubble collapse according to the numerical simulations (Fig. 2.11a). As a result, many chemical species are dissociated at the end of the bubble collapse (Fig. 2.11b). After the end of the bubble collapse (after the time for the minimum radius of a bubble), many chemical species are formed inside a bubble such as H_2, O, H_2O_2, HNO_2, and OH. In the numerical simulations, major non-condensable gas component is assumed as argon based on the argon rectification hypothesis discussed in Sect. 2.4. The amount of N_2 and O_2 inside a bubble is determined by the condition that the amount of N_2 and O_2 diffusing into a bubble by rectified diffusion balances with that dissociated inside a bubble. The chemical species present before the end of the bubble collapse in Fig. 2.11b are generated in the previous violent collapse of a stably pulsating bubble.

The amount of chemical products that dissolve into the liquid water from the interior of a SBSL bubble per acoustic cycle is listed in Table 2.1 according to the numerical simulations [17]. The dominant products are H_2, O, H_2O_2, H, HNO_2,

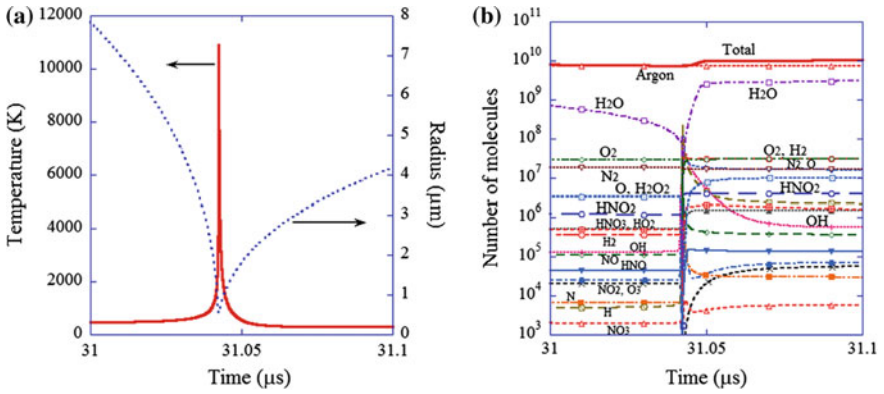

Fig. 2.11 Calculated results for a SBSL bubble in a steady state at around the end of the bubble collapse only for 0.1 μs. **a** The bubble radius and the temperature inside a bubble. **b** The number of molecules inside a bubble. Reprinted with permission from Yasui et al. [17]. Copyright (2005), AIP Publishing LLC

Table 2.1 Amount of chemical products that dissolve into the liquid water from the interior of a SBSL bubble in a steady state per acoustic cycle according to the numerical simulation

Chemical species	Number of molecules per acoustic cycle
H_2	3.1×10^7
O	1.3×10^7
H_2O_2	6.3×10^6
H	4.1×10^6
HNO_2	2.3×10^6
HO_2	1.1×10^6
HNO_3	8.4×10^5
OH	6.6×10^5
NO	2.5×10^5
HNO	9.5×10^4
NO_2	4.4×10^4
O_3	3.4×10^4
N	2.9×10^4
NO_3	3.1×10^3
N_2O	3.1×10^2

Reprinted with permission from Yasui et al. [17]. Copyright (2005), AIP Publishing LLC

HO_2, HNO_3, and OH, and the dominant oxidants are O, H_2O_2, and OH. The main oxidants in sonochemical reactions are discussed in the next section. The amount of HNO_2 of 2.3×10^6 according to the numerical simulation is considerably lower than the experimental value for NO_2^- ions (9.9×10^6) [46]. Further studies are required on this topic.

At the beginning of SBSL experiment, a bubble initially consists of air (N_2, O_2, and Ar) and water vapor. In about one hundred (100) acoustic cycles, the bubble

content gradually changes to argon (Ar) due to the argon rectification process [47]. The results of numerical simulations on an initial air bubble are shown in Fig. 2.12 [17]. The bubble temperature increases up to 6500 K at the end of the bubble collapse, which is considerably lower than that inside an argon bubble (10,900 K) because the molar heat of N_2 and O_2 is larger than that of argon. The main chemical products in an air bubble are HNO_2, HNO_3, O, H_2O_2, O_3, HO_2, NO_3, H_2, and OH (Fig. 2.12b, Table 2.2), and the main oxidants in this case are O, H_2O_2, O_3, and OH.

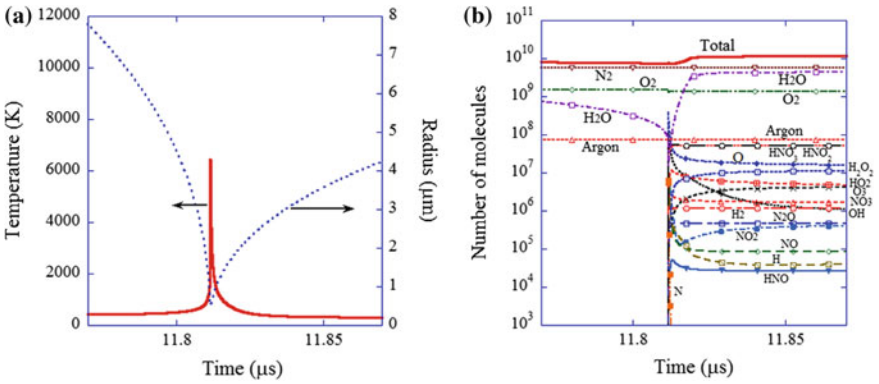

Fig. 2.12 Calculated results for an initial air bubble at around the end of the bubble collapse (only for 0.1 μs). **a** The bubble radius and the temperature inside a bubble. **b** The number of molecules inside a bubble. Reprinted with permission from Yasui et al. [17]. Copyright (2005), AIP Publishing LLC

Table 2.2 Amount of chemical products that dissolve into the liquid water from the interior of an initial air bubble in one acoustic cycle according to the numerical simulation

Chemical species	Number of molecules per acoustic cycle
HNO_2	4.0×10^7
HNO_3	3.7×10^7
O	1.6×10^7
H_2O_2	5.1×10^6
O_3	2.7×10^6
HO_2	2.3×10^6
NO_3	1.1×10^6
H_2	1.0×10^6
OH	9.9×10^5
NO_2	3.9×10^5
N_2O	3.0×10^5
NO	1.3×10^5
H	1.1×10^5
HNO	2.8×10^4
N	2.7×10^3
N_2O_5	6.8×10^2

Reprinted with permission from Yasui et al. [17]. Copyright (2005), AIP Publishing LLC

2.10 Main Oxidants

In order to study the main oxidants created inside an air bubble, numerical simulations of chemical reactions inside a pulsating bubble have been performed for several ultrasonic frequencies and pressure amplitudes [48]. The maximum bubble temperature at the end of the violent bubble collapse is plotted as a function of acoustic pressure amplitude for various ultrasonic frequencies, as shown in Fig. 2.13a [48]. For relatively low ultrasonic frequencies such as 20 and 100 kHz, a peak in the bubble temperature at relatively low acoustic amplitude is observed. The decrease in the bubble temperature as acoustic amplitude increases is due to the increase in vapor fraction inside a bubble at the end of the bubble collapse (Fig. 2.13b) [48]. Vapor fraction increases as the acoustic amplitude increases due to the larger amount of water vapor evaporating into the bubble as the bubble expands more. Because of the larger amount of water vapor at maximum bubble radius, more amount of water vapor is trapped inside a bubble at the end of the bubble collapse due to non-equilibrium condensation during the violent bubble collapse. Larger vapor fraction results in further decrease in bubble temperature because the molar heat of water vapor is larger than that of air and endothermic dissociation of water vapor inside a bubble considerably cools down the bubble. The increase of bubble temperature at low acoustic amplitude is just a result of more expansion of a bubble resulting in more violent collapse. At higher ultrasonic frequencies such as 300 kHz and 1 MHz, bubble temperature continuously increases as the acoustic amplitude increases and reaches a plateau at relatively high acoustic amplitudes. This is due to much lower vapor fraction than that at lower

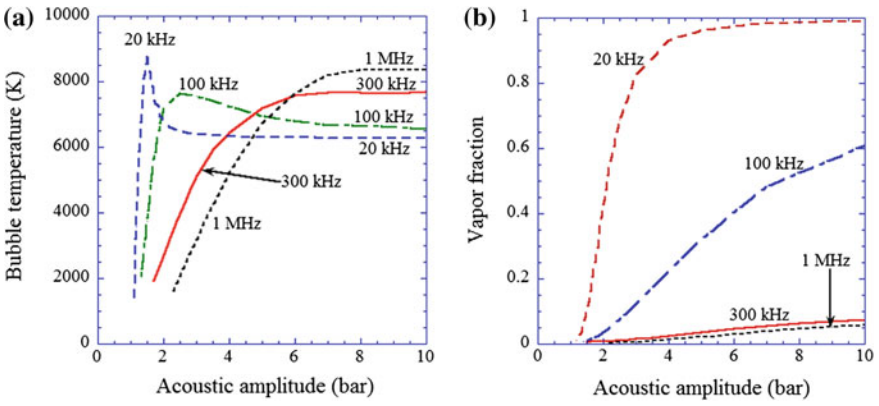

Fig. 2.13 Calculated result as a function of the acoustic amplitude for several ultrasonic frequencies (20, 100, 300 kHz, and 1 MHz) for the first collapse of an isolated spherical air bubble. The ambient bubble radii are 5 μm for 20 kHz, 3.5 μm for 100 and 300 kHz, and 1 μm for 1 MHz. **a** The temperature inside a bubble at the final stage of the bubble collapse. **b** The molar fraction of the water vapor inside a bubble at the end of the bubble collapse. Reprinted with permission from Yasui et al. [48]. Copyright (2007), AIP Publishing LLC

ultrasonic frequencies, which is caused by much smaller expansion of a bubble due to shorter period of ultrasound.

The quantity of each chemical species becomes nearly constant after about 0.05–0.1 μs after the end of the bubble collapse according to the numerical simulations shown in Figs. 2.11b and 2.12b. In Fig. 2.14, the rate of production of each oxidant inside an air bubble is estimated by the amount of each oxidant inside a bubble at about 0.05–0.1 μs after the end of the first violent collapse of the bubble. From Fig. 2.14, the quantity of oxidants at higher bubble temperatures than about 7000 K is a few orders of magnitude smaller than those at lower bubble temperatures. This is due to the consumption of oxidants inside an air bubble by oxidizing nitrogen at higher temperature than about 7000 K. Thus, there is an optimal bubble temperature for oxidant production, which is about 5500 K (Fig. 2.15a) [49]. If nitrogen

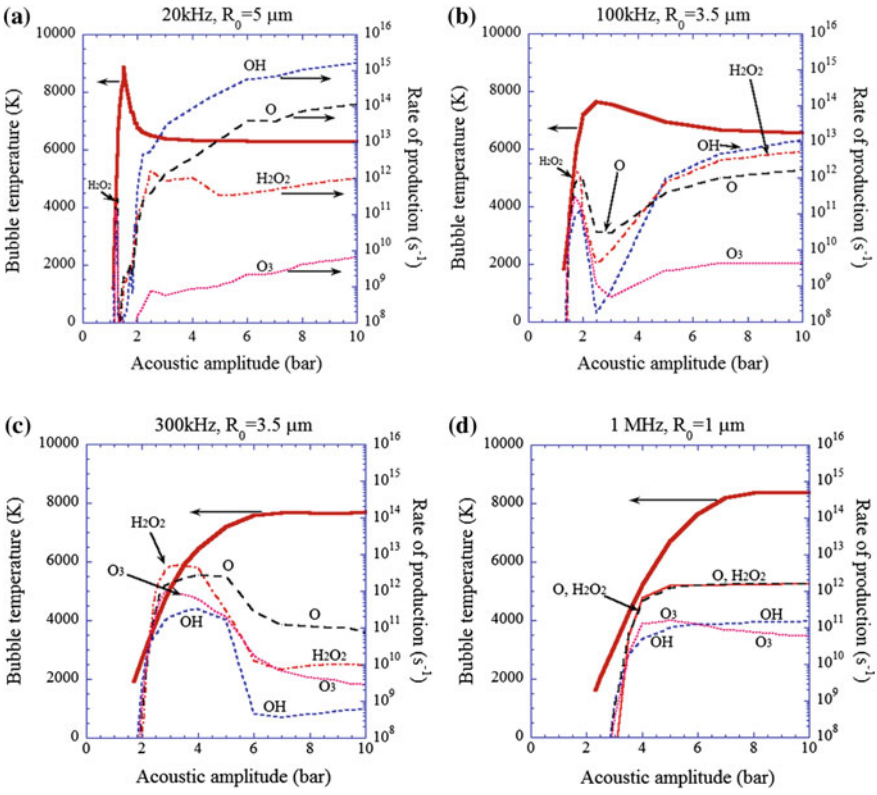

Fig. 2.14 Rate of production of each oxidant inside an isolated spherical air bubble per second calculated by the first bubble collapse as a function of acoustic amplitude with the temperature inside a bubble at the end of the bubble collapse (the thick line): **a** 20 kHz and R_0 = 5 μm. **b** 100 kHz and R_0 = 3.5 μm. **c** 300 kHz and R_0 = 3.5 μm. **d** 1 MHz and R_0 = 1 μm. Reprinted with permission from Yasui et al. [48]. Copyright (2007), AIP Publishing LLC

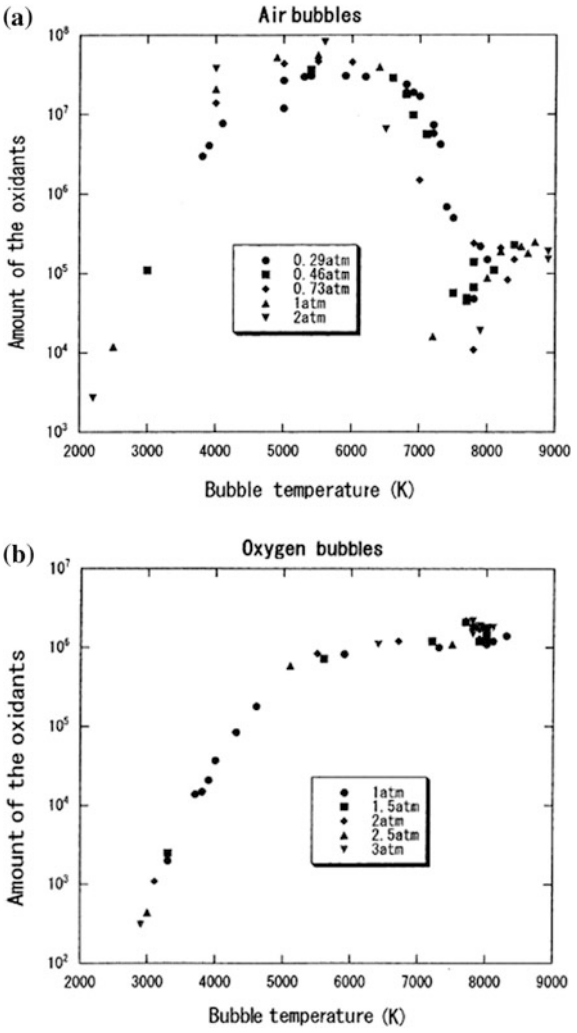

Fig. 2.15 Correlation between the bubble temperature at the collapse and the amount of the oxidants created inside a bubble per collapse. The amount of oxidants is in number of molecules. The calculated results for various ambient static pressures and various acoustic amplitudes are plotted. The ambient static pressures are indicated with the symbols. **a** For an air bubble with R_0 = 5 μm under ultrasound of 140 kHz. **b** For an oxygen bubble with R_0 = 0.5 μm under ultrasound of 1 MHz. Reprinted with permission from Yasui et al. [49]. Copyright (2004), Elsevier

(N_2) is absent, the situation completely changes such as the interior of an oxygen (O_2) bubble because the oxidants are no longer consumed there. For an oxygen bubble, the amount of oxidants created inside a bubble continuously increases as the bubble temperature increases and finally reaches a plateau at higher bubble temperatures than ∼6000 K (Fig. 2.15b) [49].

When the molar fraction of water vapor inside a bubble at the end of bubble collapse is larger than 0.5, the main oxidant is OH radical because there is a large amount of water vapor as the source of OH radicals inside a bubble (Figs. 2.13b and 2.14a, b) [48]. Furthermore, at these conditions, the bubble temperature is

lower than 7000 K, and oxidants are not excessively consumed inside a bubble. When the molar fraction of water vapor is larger than 0.5, a bubble is sometimes called *vaporous*. Thus, in vaporous bubbles, the main oxidant is OH radical.

When the molar fraction of water vapor is smaller than 0.5, a bubble is sometimes called *gaseous*. In gaseous bubbles, the main oxidant is O atom when the bubble temperature is higher than 6500 K (Fig. 2.14) [48]. When the bubble temperature is in the range of 4000–6500 K, the main oxidant is hydrogen peroxide (H_2O_2) in the gaseous bubbles (Fig. 2.14). At 1 MHz, however, H_2O_2 is one of the main oxidants even at temperatures higher than 6500 K because the duration of high temperature is too short for H_2O_2 to be dissociated inside a bubble.

The role of O atom in sonochemical reactions in solutions is still under debate [33] (see Sect. 3.9). Hart and Henglein [50] experimentally suggested that O atom contributes to KI dosimetry in sonochemical reactions as follows.

$$O + 2I^- + 2H+ \rightarrow I_2 + H_2O \tag{2.67}$$

However, there has been no direct experimental evidence on the production of O atoms in solutions (at liquid or interface regions).

2.11 Effect of Volatile Solutes

Volatile solutes such as methanol (CH_3OH) evaporate into a bubble and are dissociated inside a heated bubble near the end of a violent bubble collapse. The rate of evaporation of methanol in aqueous solution is calculated in a similar way to that of water vapor (Eqs. 2.50–2.52) as follows [51].

$$\dot{m}_{CH_3OH} = \dot{m}_{eva,CH_3OH} - \dot{m}_{con,CH_3OH} \tag{2.68}$$

$$\dot{m}_{eva,CH_3OH} = \frac{10^3 N_A}{M_{CH_3OH}} \frac{\alpha_{M,CH_3OH}}{\sqrt{2\pi R_{CH_3OH}}} \frac{p^*_{CH_3OH}}{\sqrt{T_{L,i}}} \acute{a} S_{CH_3OH} \tag{2.69}$$

$$\dot{m}_{con,CH_3OH} = \frac{10^3 N_A}{M_{CH_3OH}} \frac{\alpha_{M,CH_3OH}}{\sqrt{2\pi R_{CH_3OH}}} \frac{\Gamma_{CH_3OH} p_{CH_3OH}}{\sqrt{T_B}} \tag{2.70}$$

where M_{CH_3OH} is molecular weight of methanol (=32 g/mol), α_{M,CH_3OH} is accommodation coefficient for the evaporation or condensation for methanol, R_{CH_3OH} is the gas constant for methanol (=260 J/kg K), $p^*_{CH_3OH}$ is the saturated vapor pressure of methanol at liquid temperature ($T_{L,i}$) at the bubble wall, $\acute{a}$ is the area occupied by a methanol molecule at the gas/liquid interface (=2 × 10^{-19} m^2/molecule), S_{CH_3OH} is the instantaneous surface concentration of methanol at the bubble wall, p_{CH_3OH} is

the partial pressure of methanol inside a bubble, and the correction factor (Γ_{CH_3OH}) is calculated in a similar way to that of water vapor (Eqs. 2.53 and 2.54) as follows.

$$\Gamma_{CH_3OH} = e^{-\Omega_{CH_3OH}^2} - \Omega_{CH_3OH}\sqrt{\pi}\left[1 - \frac{2}{\sqrt{\pi}}\int_0^{\Omega_{CH_3OH}} e^{-x^2} dx\right] \tag{2.71}$$

where

$$\Omega_{CH_3OH} = \frac{\dot{m}_{CH_3OH}}{p_{CH_3OH}}\left(\frac{R_{CH_3OH}T}{2}\right)^{1/2} \tag{2.72}$$

Saturated vapor pressure of methanol is calculated as a function of the liquid temperature at the bubble wall [51]. The accommodation coefficient for methanol is assumed to be the same as that for water vapor [51].

The surface concentration of methanol at the bubble wall is calculated as follows.

$$S_{CH_3OH} = \frac{N_{S,CH_3OH}}{4\pi R^2} \tag{2.73}$$

where N_{S,CH_3OH} is the instantaneous number of methanol molecules sitting at the bubble wall. The change in number of methanol molecules at the bubble wall in time Δt is given as follows.

$$\Delta N_{S,CH_3OH} = -4\pi R^2 \dot{m}_{CH_3OH}\Delta t + \Delta N_{diff,CH_3OH} \tag{2.74}$$

where the first term is the change by evaporation or condensation at the bubble wall, and the second term is the diffusion of methanol molecules in liquid. The second term is calculated in a similar way to that for the diffusion of a non-condensable gas (Eq. 2.60) [51].

$$\Delta N_{diff,CH_3OH} = 4\pi R^2 D_{CH_3OH}\frac{A_R}{B_R}\frac{c_{\infty,CH_3OH} - c_{i,CH_3OH}}{(R_0/R)^2 R_0}\Delta t \tag{2.75}$$

where D_{CH_3OH} is the diffusion coefficient of methanol in the liquid water, c_{∞,CH_3OH} is the ambient concentration of methanol, and c_{i,CH_3OH} is the instantaneous concentration of methanol near the bubble wall.

The partial coverage of the bubble surface by methanol molecules partially inhibits evaporation and condensation of water at the bubble wall. The effective area for evaporation and condensation of water is reduced from $4\pi R^2$ to $4\pi R^2(1 - \acute{a}S_{CH_3OH})$.

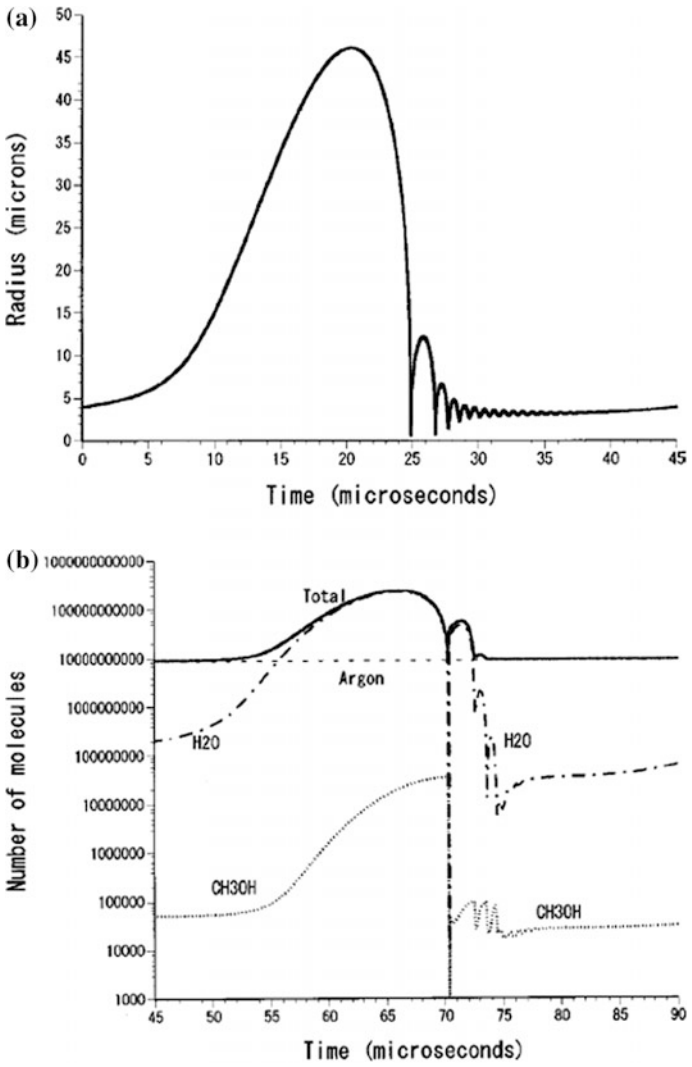

Fig. 2.16 Calculated results of an argon bubble in aqueous methanol solution [$S_{eq} = 0.01 \times 10^{14}$ (molecules/cm^2), where S_{eq} is the equilibrium surface concentration of methanol] as a function of time for one acoustic cycle (45 μs) when the frequency and amplitude of ultrasound are 22 kHz and 1.32 bar, respectively, and the ambient bubble radius is 4 μm. **a** Bubble radius. **b** Number of molecules inside a bubble with logarithmic scale. Reprinted with permission from Yasui [51]. Copyright (2002), AIP Publishing LLC

The change in number of methanol molecules inside a bubble (n_{CH_3OH}) is calculated as follows.

$$n_{CH_3OH}(t+\Delta t) = n_{CH_3OH}(t) + 4\pi R^2 \dot{m}_{CH_3OH}\Delta t - \frac{4}{3}\pi R^3 r_{CH_3OH+M\rightarrow CH_3+OH+M}\Delta t \tag{2.76}$$

where $r_{CH_3OH+M\rightarrow CH_3+OH+M}$ is the rate of the following chemical reaction.

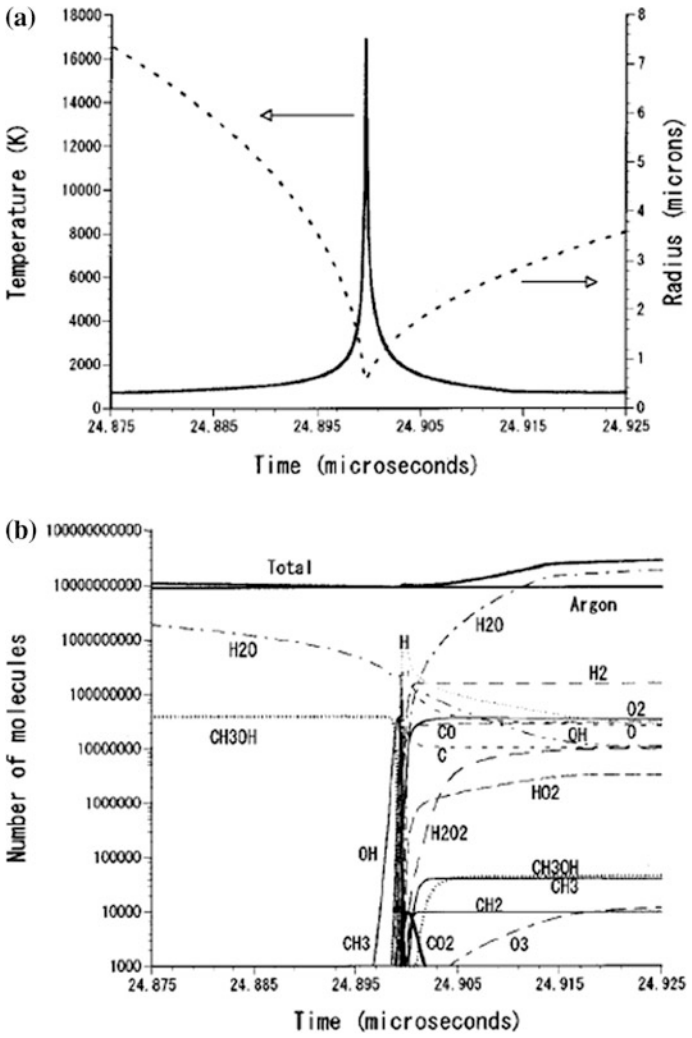

Fig. 2.17 Calculated results at around the minimum bubble radius in aqueous methanol solution. The condition is the same as that in Fig. 2.16. **a** Bubble radius and temperature inside a bubble. **b** Number of molecules inside a bubble with logarithmic scale. Reprinted with permission from Yasui [51]. Copyright (2002), AIP Publishing LLC

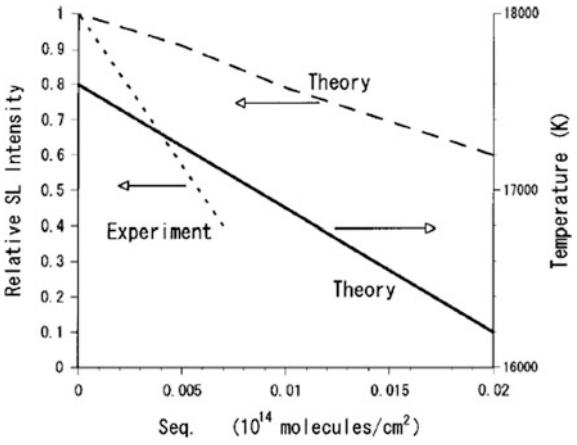

Fig. 2.18 Energy of the emitted light per bubble collapse and the bubble temperature at the collapse as a function of equilibrium surface concentration of methanol (S_{eq}). The experimental data of the relative sonoluminescence intensity (Ref. [52]) are also shown. Reprinted with permission from Yasui [51]. Copyright (2002), AIP Publishing LLC

$$CH_3OH + M \rightarrow CH_3 + OH + M \tag{2.77}$$

where M is a third body.

In the calculation of the temporal change in the internal thermal energy of a bubble (Eq. 2.49), an additional term accounting energy change due to evaporation or condensation of methanol should be added.

Results of the numerical simulations are shown in Figs. 2.16, 2.17, and 2.18 under a condition of single-bubble sonoluminescence (SBSL) and argon rectification (Sect. 2.4) [51]. Methanol evaporates into a bubble during bubble expansion and condenses at the bubble wall during bubble collapse like water vapor (Fig. 2.16). At the end of a violent bubble collapse, most of the methanol molecules inside a bubble are dissociated due to high temperatures (Fig. 2.17). As a result, the maximum bubble temperature at the collapse decreases as the methanol concentration increases because the endothermic dissociation of methanol considerably cools down a bubble (Fig. 2.17). However, the calculated relative SL intensity is higher than the experimental data (Fig. 2.18) [51, 52]. It is probably due to the accumulation of chemical products by the dissociation of methanol inside a bubble, which is not taken into account in the present numerical simulations [53].

2.12 Resonance Radius

The Rayleigh–Plesset equation as well as the Keller equation is a nonlinear equation because there are nonlinear terms such as $R\ddot{R}$ and $\dot{R}^2$. The linear equation is defined as the equation which satisfies the following superposition principle.

$$f(\alpha x_1 + \beta x_2) = \alpha f(x_1) + \beta f(x_2) \tag{2.78}$$

where f is a function of x, x_1 and x_2 are arbitrary values of x, and α and β are arbitrary constants. If a function f does not satisfy Eq. (2.78), it is a nonlinear function. For example, a function f defined by $f(R) = R + \ddot{R}$ is a linear function because $f(\alpha R_1 + \beta R_2) = \alpha f(R_1) + \beta f(R_2)$. On the other hand, a function f defined by $f(R) = R\ddot{R}$ is a nonlinear function because

$$f(\alpha R_1 + \beta R_2) = (\alpha R_1 + \beta R_2) \cdot \left(\alpha \ddot{R}_1 + \beta \ddot{R}_2\right) \neq \alpha f(R_1) + \beta f(R_2) \tag{2.79}$$

Generally speaking, a linear function of x consists only of a first-order term (ax, where a is a constant) and a constant. Other functions are nonlinear such as a function containing higher order terms (bx^2, cx^3, etc.).

Any radius–time curve $(R(t))$ can be expressed by the non-dimensional function $x(t)$ defined as follows.

$$R(t) = R_0(1 + x(t)) \tag{2.80}$$

$x(t)$ means degree of deviation of $R(t)$ from the ambient value R_0. Now let us consider very weak pulsation of a bubble so that $|x(t)| \ll 1$. In this case, $1 \gg |x(t)| \gg |x(t)|^2$ holds. Thus, in the Rayleigh–Plesset equation, only the first-order terms need to be considered. Inserting Eq. (2.80) into the Rayleigh–Plesset equation (Eq. 2.12) gives the following equation (by neglecting the higher order terms).

$$\ddot{x} + 2\gamma_{\mathrm{d}}\dot{x} + \omega_0^2 x = f_0 \sin \omega t \tag{2.81}$$

where

$$\gamma_{\mathrm{d}} = \frac{2\mu}{\rho_0 R_0^2} \tag{2.82}$$

$$\omega_0 = \frac{1}{R_0}\sqrt{\frac{\left[3\gamma p_0 + (3\gamma - 1)\frac{2\sigma}{R_0}\right]}{\rho_0}} \tag{2.83}$$

$$f_0 = \frac{A}{\rho_0 R_0^2} \tag{2.84}$$

In the derivation, the bubble pulsation is assumed to be adiabatic as follows.

$$p_{\mathrm{g}}(t) = \left(p_0 + \frac{2\sigma}{R_0}\right)\left(\frac{R}{R_0}\right)^{-3\gamma} \tag{2.85}$$

where γ is ratio of specific heats ($\gamma = 1.4$ for air, 1.67 for argon). Furthermore, the vapor pressure (p_v) and the Laplace pressure $\left(\frac{2\sigma}{R_0}\right)$ are neglected compared to the acoustic pressure amplitude (A). Equation (2.81) is an equation for a forced oscillator with a natural frequency ω_0 and with damping constant γ_d.

Solution of Eq. (2.81) is given as follows [54]:

$$x = ae^{-\gamma_d t}\cos(\omega_\gamma + \alpha) + \frac{f_0}{\sqrt{\left(\omega_0^2 - \omega^2\right)^2 + (2\gamma_d\omega)^2}}\sin(\omega t + \varphi) \tag{2.86}$$

where a is a constant. $\omega_\gamma = \sqrt{\omega_0^2 - \gamma_d^2}$, where $\omega_0 > \gamma_d$ is used. α is a constant and φ is given as follows.

$$\varphi = \tan^{-1}\frac{-2\gamma_d\omega}{\omega_0^2 - \omega^2} = \tan^{-1}\left[\frac{-2F\Gamma_\gamma}{(1-F^2)}\right] \tag{2.87}$$

where F and Γ_γ are defined as follows.

$$F = \frac{\omega}{\omega_0} \tag{2.88}$$

$$\Gamma_\gamma = \frac{\gamma_d}{\omega_0} \tag{2.89}$$

The first term on right-hand side of Eq. (2.86) becomes negligible after a sufficient time as $e^{-\gamma_d t} \to 0$ with $t \to \infty$. Then, the amplitude of oscillation (A_1) is given as follows.

$$A_1 = \frac{A_0}{\sqrt{(1-F^2)^2 + 4\Gamma_\gamma^2 F^2}} \tag{2.90}$$

where $A_0 = \frac{f_0}{\omega_0^2}$.

The results of the numerical calculations of Eqs. (2.87) and (2.90) are shown in Fig. 2.19 for an air bubble in water at 20 °C. The amplitude of oscillation has a sharp peak at $\omega = \omega_0$ for both the ambient radii of 1 and 1000 μm. Thus, the frequency given by Eq. (2.83) is called (linear) resonance frequency ($= \frac{\omega_0}{2\pi}$) which is shown in Fig. 2.20. The resonance frequency decreases as the ambient bubble radius (R_0) increases from 4750 kHz at $R_0 = 1$ μm to 3.29 kHz at $R_0 = 1000$ μm. As the effect of viscosity (damping) becomes weaker as the ambient bubble radius increases, the peak in amplitude of oscillation becomes higher (Fig. 2.19a). With regard to the phase difference between the driving ultrasound and the bubble oscillation (Eq. 2.87 in Fig. 2.19b), ultrasound and the bubble oscillation are in phase (no phase difference) when the driving frequency is much lower than the resonance frequency of a bubble ($F \sim 0$). On the other hand, ultrasound and bubble

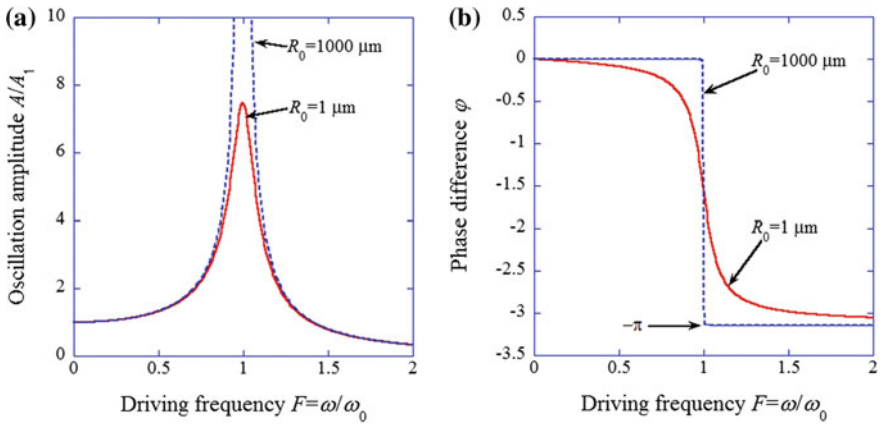

Fig. 2.19 Oscillation amplitude (Eq. 2.90) (**a**) and phase difference (Eq. 2.87) (**b**) as a function of the driving frequency in a forced oscillator (bubble pulsation)

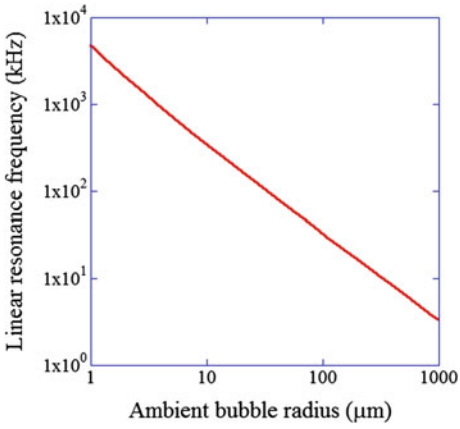

Fig. 2.20 Linear resonance frequency of a bubble as a function of the ambient radius

oscillation are in anti-phase (a phase difference of $-\pi$) when the driving frequency is much higher than the resonance frequency ($F \gg 1$). For larger ambient bubble radius, this behavior is more significant due to negligible effect of damping (Fig. 2.19b).

However, the bubble pulsation in acoustic cavitation is strongly nonlinear. The linear approximation is valid only for very low acoustic amplitudes. As shown in Fig. 2.21, the peak in the expansion ratio (R_{max}/R_0, where R_{max} is the maximum radius of a pulsating bubble) is at about $R_0 = 6$ μm for an acoustic amplitude of 0.5 bar ($= 5 \times 10^4$ Pa = 0.493 atm) at 300 kHz, which is considerably smaller than the linear resonance radius of 11.4 μm (Eq. 2.83) [43]. For an acoustic amplitude of 3 bar, the peak is at about 0.4 μm, which is more than one order of magnitude smaller than the linear resonance radius. For this acoustic amplitude, a

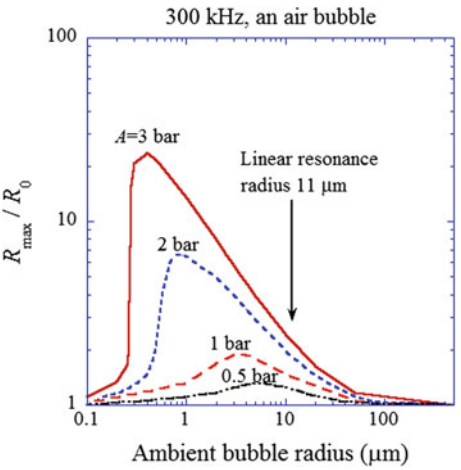

Fig. 2.21 Calculated expansion ratio (R_{max}/R_0) as a function of the ambient bubble radius for various acoustic amplitudes at 300 kHz. Both the horizontal and vertical axes are in logarithmic scale. Reprinted with permission from Yasui et al. [43]. Copyright (2008), AIP Publishing LLC

bubble significantly expands ($R_{max}/R_0 > 3$) in the range of 0.27 μm < R_0 < 7 μm [43]. In other words, a bubble actively pulsates for a wide range of ambient radius which does *not* include the linear resonance radius of 11.4 μm. This means that at this acoustic amplitude, a bubble of linear resonance size is *inactive* due to the nonlinearity of bubble pulsation. The ambient radius for the peak in expansion ratio is sometimes called *nonlinear* resonance radius. The peak is not sharp, and a bubble strongly pulsates in a wide range of ambient radius. The upper bound of the ambient radius for an active bubble is in the same order of magnitude as the linear resonance radius (Fig. 2.22) [43]. The lower bound nearly coincides with the *Blake threshold* radius given as follows [2, 39].

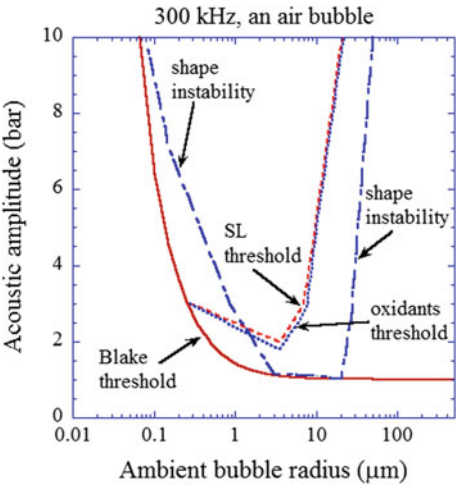

Fig. 2.22 Calculated thresholds for shape instability, sonoluminescence (SL), and oxidant production as well as the Blake threshold (Eq. 2.91) in $R_0 - A$ plane. Reprinted with permission from Yasui et al. [43]. Copyright (2008), AIP Publishing LLC

$$p_{\mathrm{Blake}} = p_0 + \frac{8\sigma}{9}\sqrt{\frac{3\sigma}{2R_{0,\mathrm{Blake}}^3\left[p_0 + \left(2\sigma/R_{0,\mathrm{Blake}}\right)\right]}} \tag{2.91}$$

where p_{Blake} is the pressure amplitude of ultrasound (the Blake threshold pressure for transient cavitation), and $R_{0,\mathrm{Blake}}$ is the ambient bubble radius (the Blake threshold radius). The Blake threshold pressure is a threshold above which a bubble significantly expands (and subsequently collapses). The derivation of Eq. (2.91) is given in Ref. [2].

2.13 Shock Wave Emission

The Mach number (M) is defined as the fluid velocity divided by the sound velocity. A shock wave is a propagation of a discontinuity in pressure in a medium [10, 55]. For a shock wave propagating in a homogeneous medium under steady-state conditions, upstream velocity of fluid is normally higher than sound velocity ($M > 1$) according to the *Rankine–Hugoniot* relations [10]. It is also known that a shock wave is emitted when the velocity of an airplane exceeds sound velocity. Generally speaking however, shock wave can be emitted even when the Mach number is less than 1. An example is shock wave emission from a bubble at its collapse. Figure 2.23 shows a photograph of a spherical shock wave emitted from a bubble at its collapse [56]. The circle in Fig. 2.23 is the spherical shock wave propagating outward from the center of a circle where a bubble is present although it is invisible in the photograph.

The reason for the shock wave emission from a bubble can be understood from a result of numerical simulations (Figs. 2.24 and 2.25) [57]. As shown in Fig. 2.24a, b, the shock formation occurs during rebounding of a bubble after a violent collapse.

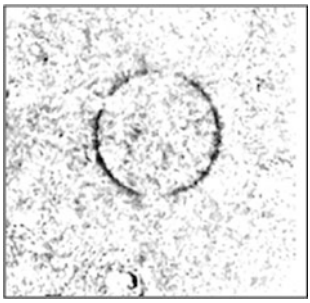

Fig. 2.23 An image of a spherical shock wave emitted by a sonoluminescing bubble. At 480 ns after the bubble collapse. The side length of the image is 3.5 mm. Reprinted with permission from Holzfuss et al. [56]. Copyright (1998), American Physical Society

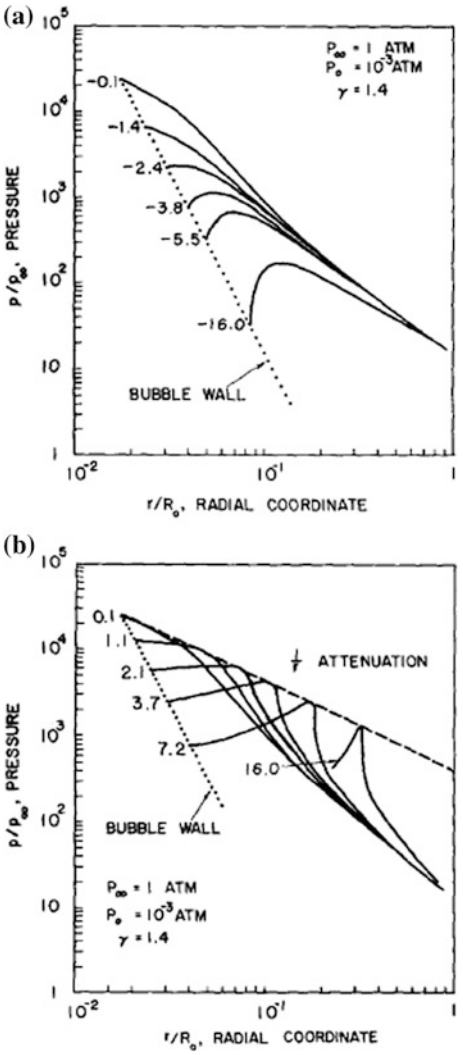

Fig. 2.24 Variation of pressure with distance from the bubble wall at various instances in time. **a** During the collapse of a bubble. **b** During the rebound of a bubble. Reprinted with permission from Hickling and Plesset [57]. Copyright (1964), AIP Publishing LLC

Just after a violent collapse, a bubble starts expanding. However, the liquid slightly apart from a bubble still flows toward a bubble (the velocity is still negative) (e.g., at time 0.1 after the end of the collapse in Fig. 2.25, the fluid velocity (Mach number) is negative at a region slightly away from a bubble wall). Furthermore, the sound velocity decreases as the distance from a bubble increases because the liquid pressure decreases (the sound velocity decreases as the liquid pressure decreases). The pressure wave continuously emitted from an expanding bubble propagates with the speed equivalent to the sum of the sound velocity and the fluid (liquid) velocity. Due to the above two factors, the pressure waves radiated from an expanding bubble

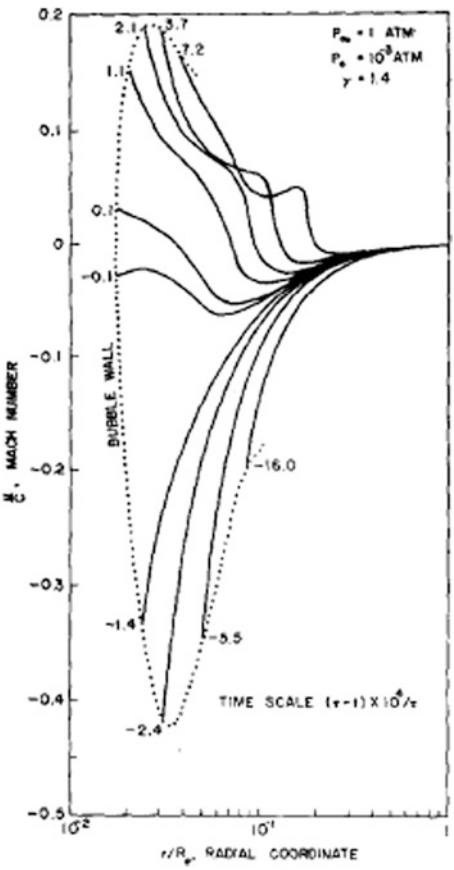

Fig. 2.25 Variation of the Mach number with distance from the bubble wall at different instances in time during the collapse and rebound of a bubble. Reprinted with permission from Hickling and Plesset [57]. Copyright (1964), AIP Publishing LLC

overtake the previously radiated pressure waves. In this way, a shock wave is formed as seen as a pressure peak propagating outward as shown in Fig. 2.24b. It should be noted that the absolute value of the Mach number of the bubble wall is much less than 1 during the formation of the shock wave (Fig. 2.25) [54].

2.14 Shock Formation Inside a Bubble

According to some numerical simulations of fundamental equations of fluid dynamics *inside* a collapsing bubble, a spherical shock wave is formed, which propagates inwardly and finally focuses at the bubble center [58–60]. When a spherical shock wave focuses at the bubble center, temperature increases to about 10^6 K (1,000,000 K) or more. However, other numerical simulations taking into account the effect of thermal conduction inside a collapsing bubble have revealed

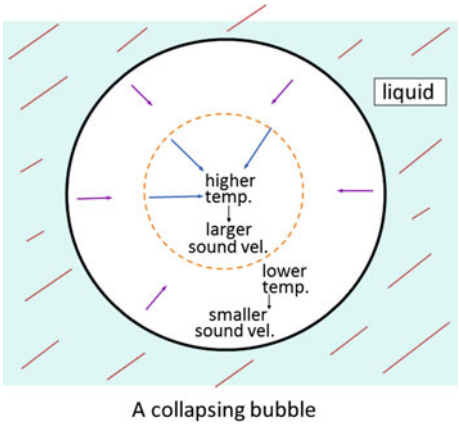

Fig. 2.26 Difficulty in shock wave formation inside a collapsing bubble. Reprinted with permission from Yasui [2]. Copyright (2015), Elsevier

that no shock wave is formed and that temperature and pressure are almost spatially uniform except near the bubble wall inside a collapsing bubble [61–65].

The reason of no shock formation is as follows (Fig. 2.26) [2, 66]. Due to the thermal conduction from the hotter bubble interior to the colder bubble wall, the temperature increases as the distance from the bubble wall increases toward the center of a bubble. As the sound velocity increases as temperature increases, the sound velocity increases as the distance from the bubble wall increases toward the center of a bubble. The pressure waves radiated from the bubble wall inside a bubble toward the center of a bubble propagate with the speed equivalent to the sum of the sound velocity and the fluid (gas) velocity. As the sound velocity increases as the distance from the bubble wall increases, the pressure waves barely overtake the previously radiated pressure waves inside a collapsing bubble. Thus, the shock wave is barely formed inside a collapsing bubble.

2.15 Jet Penetration Inside a Bubble

When the pressure field around a bubble is strongly asymmetric, a liquid jet penetrates into a collapsing bubble. It is most often observed for the bubble collapse near a solid surface (Figs. 2.27 and 2.28) [67, 68]. Just before the bubble collapse near a solid surface, the liquid pressure on the bubble surface near a solid boundary becomes much lower than that on the other side of the bubble surface (Fig. 2.28) [68]. As a result, a jet penetrates into a bubble and finally hits the solid surface. Then, the liquid flow spreads on the solid surface and cleans the surface (contaminated with small particles) (Fig. 2.29d) [67]. During the bubble expansion (Fig. 2.29a) and bubble collapse (Fig. 2.29b), fluorescent particles of 8 μm in diameter initially distributed on the solid surface moved associated with the liquid flow due to bubble pulsation. However, the permanent displacement of particles

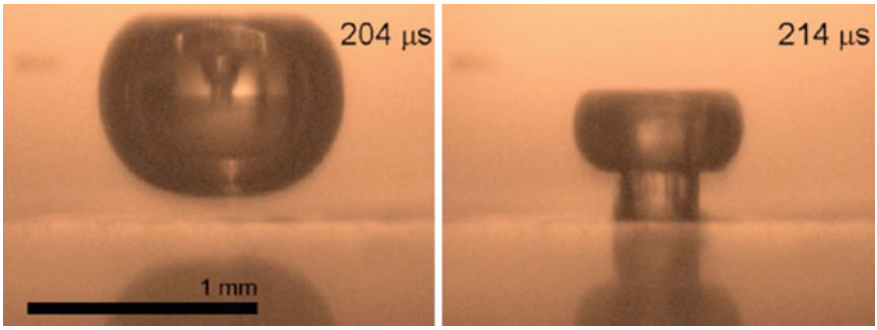

Fig. 2.27 Stroboscopic pictures visualizing liquid jet within a bubble (left) and impacting on the solid boundary (right). The bubble was generated by focusing an intense laser pulse of 1064 nm in wavelength and 6 ns in duration. Reprinted with permission from Ohl et al. [67]. Copyright (2006), AIP Publishing LLC

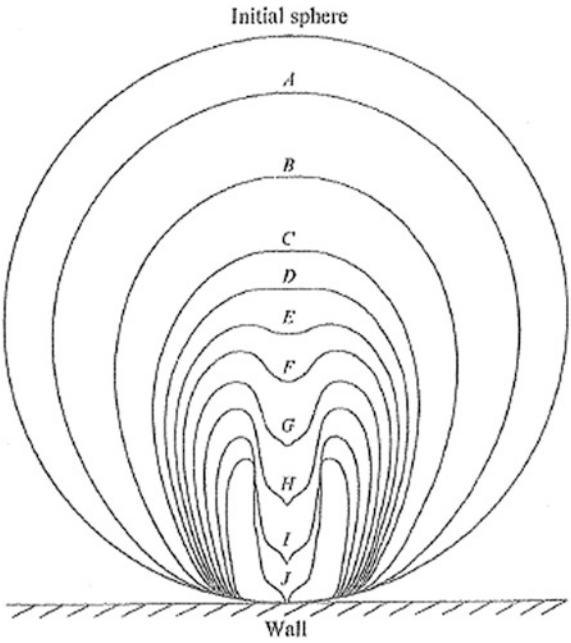

Fig. 2.28 Results of numerical simulations for the collapse of an initially spherical bubble near a plane solid wall when the bubble boundary was in contact with the solid wall. Reprinted with permission from Plesset and Chapman [68]. Copyright (1971), Cambridge University Press

was observed only during the jet impact (from Fig. 2.29c, d) [67]. A jet impact also causes a damage of the solid surface (Fig. 2.30) [69].

Jet penetration also occurs when two neighboring bubbles simultaneously collapse (Fig. 2.31) [70]. Another situation of jet penetration into a bubble is the bubble collapse in a traveling ultrasonic wave [71].

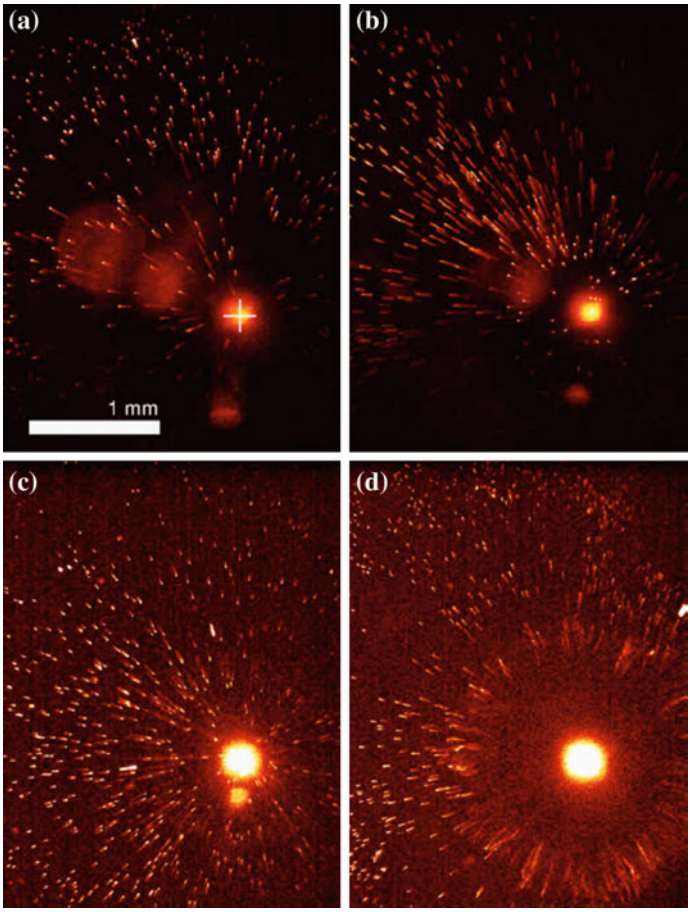

Fig. 2.29 Photograph of the particle streaks **a** during the bubble expansion, **b** during the bubble collapse, **c** during the jet impact, and **d** during re-expansion of the bubble. The position of the bubble center is indicated with a cross in (**a**). Reprinted with permission from Ohl et al. [67]. Copyright (2006), AIP Publishing LLC

2.16 Radiation Forces (Bjerknes Forces)

The radiation forces on a bubble in liquid under ultrasound originate in pressure inhomogeneity around a bubble. If the pressure inhomogeneity originates in an external acoustic field (driving ultrasound), the radiation force is called *primary Bjerknes force*. If it originates in an acoustic wave radiated by a neighboring bubble, it is called *secondary Bjerknes force*. Both primary and secondary Bjerknes forces are principally expressed by the same equation as follows [72].

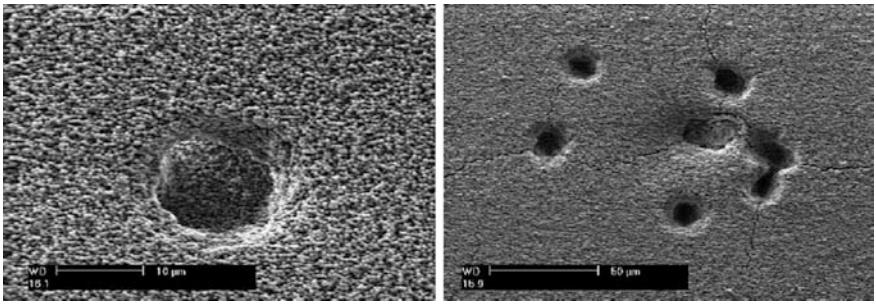

Fig. 2.30 SEM images showing evidence of microjet impacts on the surface of the cake layer made of sulfate polystyrene latex particles of 0.53 μm in average diameter. Left: ultrasound operating at 1062 kHz for 5 s and 0.21 W/cm^2. Right: ultrasound operating at 620 kHz for 5 s and 0.12 W/cm^2. Reprinted with permission from Lamminen et al. [69]. Copyright (2004), Elsevier

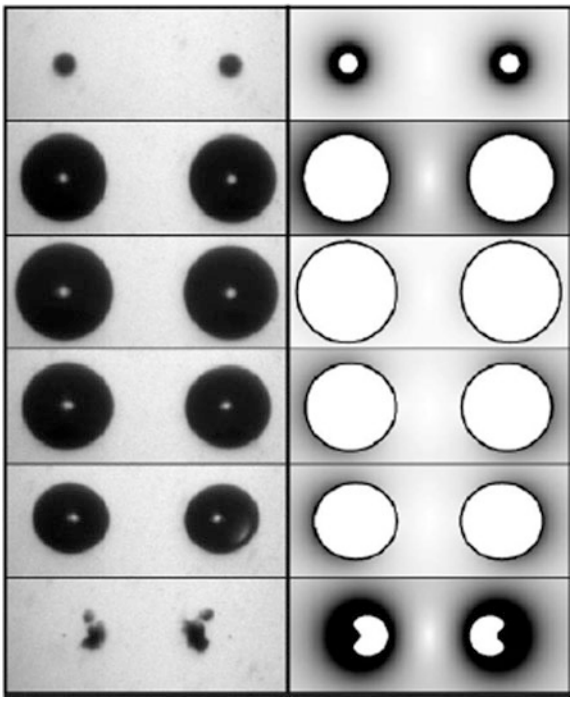

Fig. 2.31 Comparison between experimental and simulation of the cavitation of two bubbles initially set at a distance of 400 μm subjected to a minimum pressure of −1.4 MPa. Each time step is 4 μs in the direction from the top to the bottom (the total time is 20 μs). Reprinted with permission from Bremond et al. [70]. Copyright (2006), AIP Publishing LLC

$$\vec{F}_{\mathrm{B}} = \left\langle \vec{F}_{\mathrm{p}} \right\rangle = -\left\langle V \vec{\nabla} p \right\rangle \tag{2.92}$$

where $\vec{F}_{\mathrm{B}}$ is the primary or secondary Bjerknes force, $\vec{F}_{\mathrm{p}}$ is the instantaneous radiation force which dramatically changes in one acoustic cycle including direction of the force, $\langle\ \rangle$ means the time-averaged value, V is the instantaneous bubble

volume, $\vec{\nabla} = \left(\frac{\partial}{\partial x}, \frac{\partial}{\partial y}, \frac{\partial}{\partial z}\right)$, and $p = p(x, y, z, t)$ is the instantaneous pressure field around a bubble.

Firstly, the primary Bjerknes force in a standing acoustic field is discussed. As an example, the instantaneous pressure field is given as follows.

$$p(z,t) = -A\cos(kz)\sin(\omega t) \tag{2.93}$$

where A is the pressure amplitude of ultrasound, and the origin ($z = 0$, $t = 0$) has been appropriately shifted compared to Eq. (1.28). When a liquid is irradiated with ultrasound by a transducer attached at the bottom ($z = 0$) of a liquid container, a standing wave field is formed as given by Eq. (2.93) if the liquid height is at $z = (2n+1)\pi/2k$, where z-axis is in the vertical direction and n is a natural number. Then, instantaneous radiation force is given as follows.

$$\vec{F}_{\mathrm{p}} = (-4\pi/3)R^3 kA\sin(kz)\sin(\omega t)\vec{e}_z \tag{2.94}$$

where R is instantaneous bubble radius, and $\vec{e}_z$ is a unit vector in z direction. In Fig. 2.32a, the bubble radius as well as the acoustic pressure is shown as function of time at 20 kHz [73]. A bubble is slightly off the pressure antinode (by 1 mm) in the calculation. During the rarefaction phase of ultrasound, over the initial

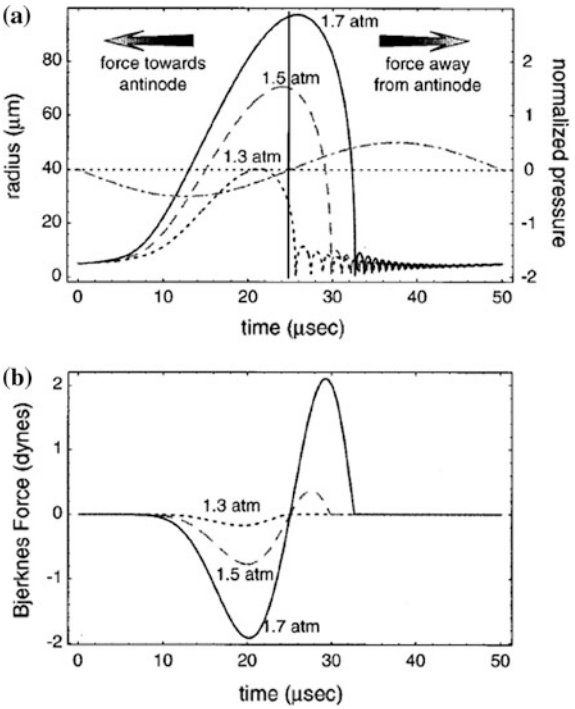

Fig. 2.32 **a** Calculated steady-state radius–time curves for a 5-μm bubble driven with a pressure amplitude of 1.3, 1.5, and 1.7 atm. Note that as the pressure amplitude is increased, the bubble collapses later in the acoustic cycle, such that it remains relatively large even after the pressure changes phase. The arrows illustrate the direction of the Bjerknes force, toward the pressure antinode during the first half cycle and away from the pressure antinode during the second half cycle. **b** The instantaneous radiation force for bubbles driven as shown in (**a**). Reprinted with permission from Matula et al. [73]. Copyright (1997), AIP Publishing LLC

half-wave period (0–25 μs), a bubble expands. At this stage, the instantaneous acoustic pressure is lowest at pressure antinode, and the instantaneous radiation force is directed toward the pressure antinode. [The instantaneous radiation force is directed toward lower pressure region as indicated in Eq. (2.92).] In the compression phase of ultrasound during the latter half-wave period (25–50 μs), a bubble collapses and undergoes bouncing motion. At this stage, the instantaneous acoustic pressure is highest at pressure antinode, and the instantaneous radiation force is directed away from pressure antinode. As the instantaneous radiation force is proportional to bubble volume (Eq. 2.92), the force is stronger during bubble expansion compared to that during bubble collapse (Fig. 2.32b). As a result, time-averaged radiation pressure (primary Bjerkens force) is directed toward the pressure antinode. However, when the acoustic pressure amplitude is higher than about 1.8 bar at 20 kHz, bubble expansion still continues at the beginning of compression phase of ultrasound. This gives rise to a repulsive force from the pressure antinode in the compression phase that is stronger than the attractive one generated during the rarefaction phase. Consequently, a bubble is repelled from the pressure antinode above about 1.8 bar at 20 kHz [73]. This behavior is seen in the experimental observation of the bubble structure in Fig. 1.11.

Next, the primary Bjerknes force in a traveling acoustic wave is discussed. In this case, instantaneous pressure field is given as follows as in Eq. (1.2).

$$p(z,t) = -A(z)\sin(\omega t - kz) \tag{2.95}$$

where the acoustic pressure amplitude A is a function of position z as in the case of an acoustic field under an ultrasonic horn (probe) (Eq. 1.13), and then, the instantaneous radiation force is given as follows.

$$\vec{F}_{\mathrm{p}} = (4\pi/3)R^3 \sin(\omega t - kz)\vec{\nabla}A - (4\pi/3)AkR^3 \cos(\omega t - kz)\vec{e}_z \tag{2.96}$$

In many cases, time-averaged $\vec{F}_{\mathrm{p}}$ is directed away from a horn tip [74].

Finally, the secondary Bjerknes force is discussed [75].

$$\vec{F}_{1\to 2} = -V_2 \vec{\nabla} p_1 \tag{2.97}$$

where $\vec{F}_{1\to 2}$ is the force acting on bubble 2 from bubble 1, V_2 is the volume of bubble 2, and p_1 is the acoustic pressure radiated from bubble 1. The pulsating bubble radiates acoustic wave into the surrounding liquid. Let us consider the Euler equation (equation of motion) in fluid dynamics already discussed in Eq. (2.16).

$$\frac{\partial \vec{u}}{\partial t} + (\vec{u}\cdot\nabla)\vec{u} = -\frac{1}{\rho}\nabla p \tag{2.98}$$

The fluid (liquid) velocity $(\vec{u})$ around a pulsating bubble is given by Eq. (2.99) according to the condition of incompressibility of liquid [described below Eq. (2.2)].

$$\vec{u} = \frac{R^2 \dot{R}}{r^2} \vec{e}_{\mathrm{r}} \tag{2.99}$$

where $\vec{e}_{\mathrm{r}}$ is a radial unit vector with its origin at the center of a bubble. Then, the second term on the left-hand side of Eq. (2.98) is proportional to r^{-5} and negligible compared to the first term. Inserting Eq. (2.99) into Eq. (2.98) yields Eq. (2.100).

$$\frac{\partial p}{\partial r} = -\frac{\rho}{r^2} \frac{\mathrm{d}}{\mathrm{d}t} \left(R^2 \dot{R} \right) \tag{2.100}$$

where p is the acoustic pressure radiated from a bubble. Integrating Eq. (2.100) with r yields Eq. (2.101).

$$p = \frac{\rho}{r} \frac{\mathrm{d}}{\mathrm{d}t} \left(R^2 \dot{R} \right) = \frac{\rho}{4\pi r} \frac{\mathrm{d}^2 V}{\mathrm{d}t^2} \tag{2.101}$$

where $V = \frac{4}{3}\pi R^3$ is the instantaneous volume of a bubble. Inserting Eq. (2.101) into Eq. (2.97) yields Eq. (2.102).

$$\vec{F}_{1 \to 2} = \frac{\rho}{4\pi d^2} \left\langle \ddot{V}_1 V_2 \right\rangle \vec{e}_{1 \to 2} \tag{2.102}$$

where d is the distance between the bubble centers of bubbles 1 and 2, V_1 and V_2 are the volumes of bubbles 1 and 2, respectively, $\ddot{V}_1 = \frac{\mathrm{d}^2 V_1}{\mathrm{d}t^2}$, and $\vec{e}_{1 \to 2}$ is a unit vector directed from bubble 1 to bubble 2. When the coefficient of $\vec{e}_{1 \to 2}$ in Eq. (2.102) is negative, the secondary Bjerknes force is attractive.

In Fig. 2.33, the coefficient for the secondary Bjerknes force (coefficient of $\vec{e}_{1 \to 2}$) is shown for various combinations of ambient radii of bubbles 1 and 2 at 20 kHz

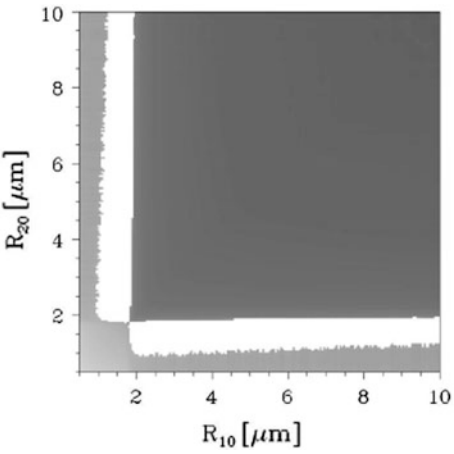

Fig. 2.33 Coefficient for the secondary Bjerknes force (coefficient of $\vec{e}_{1 \to 2}$). The horizontal and vertical axes are ambient radii of bubble 1 and 2, respectively. The black (white) region shows attractive (repulsive) secondary Bjerknes force. Reprinted with permission from Mettin et al. [75]. Copyright (1997), American Physical Society

and 1.32 bar according to numerical calculations [75]. The black (white) region shows that the secondary Bjerkens force is attractive (repulsive). For most combinations of ambient radii, the secondary Bjerkens force is attractive. However, when one of the bubbles has a relatively small ambient radius (1–2 μm), the secondary Bjerknes force is repulsive if the ambient radius of the other bubble is larger.

2.17 Effect of Salts and Surfactants

Bubble–bubble coalescence is strongly retarded by the presence of surfactants, salts, alcohols, and sugars (e.g., glucose) above certain concentrations [76–80]. In other words, coalescence of bubbles is largely inhibited if solute concentration is above a critical one which is often called *transition concentration*. Different mechanisms have been proposed to explain the inhibition of coalescence of bubbles in the presence of various solutes [76]. However, there is no consensus on a mechanism which can explain the inhibition of coalescence of bubbles for all such solutes. However, one of many promising mechanisms is described as follows. Let us consider a liquid film between two coalescing bubbles (Fig. 2.34). For coalescence to be completed, a liquid film should be ruptured. In the presence of solutes, thinning of a liquid film which is necessary for its rupture could be inhibited by higher surface tension at center of a film compared to that at the edge of a film. The difference in surface tension originates in gradient of concentration of solutes along the film. The difference in surface tension may be expressed as follows [77, 81–83].

$$\Delta\sigma = -\frac{1}{\nu h}\left(\frac{2c_{\text{solute}}}{\mathrm{R_g}T_{\mathrm{L}}}\right)\left(\frac{\partial\sigma}{\partial c_{\text{solute}}}\right)^2 \tag{2.103}$$

where $\Delta\sigma$ is the surface tension at the edge of a film minus that at the film center, ν is the number of ions produced upon dissociation when the solute is electrolyte, h is the thickness of a liquid film (Fig. 2.34), c_{solute} is the solute concentration, $\mathrm{R_g}$ is the universal gas constant, and T_{L} is the liquid temperature. Surface tension at the film center is higher than that at the edge of a film because Eq. (2.103) is always

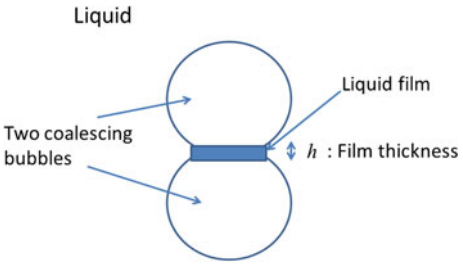

Fig. 2.34 Two coalescing bubbles

negative. It works against thinning of a liquid film. The magnitude of the difference in surface tension is proportional to $\left(\frac{\partial\sigma}{\partial c_{\text{solute}}}\right)^2$. It has been reported that the experimental transition concentration is well correlated with $\left(\frac{\partial\sigma}{\partial c_{\text{solute}}}\right)^2$ (or equivalently with $\left(\frac{\partial\sigma}{\partial c_{\text{solute}}}\right)^{-2}$) [80]. Further studies are required on the mechanism of inhibition of bubble coalescence by solutes above transition concentration.

In acoustic cavitation, bubble–bubble coalescence frequently occurs by attractive secondary Bjerknes forces [38]. As a result, larger bubbles are frequently formed, and average bubble size gradually increases although some of the bubbles are fragmented into smaller "daughter" bubbles [84, 85]. In the presence of solutes above a certain concentration, bubble–bubble coalescence is largely inhibited even in acoustic cavitation. As a result, number of tiny active bubbles increases as larger inactive bubbles are seldom formed. It has been experimentally reported that sonoluminescence intensity increases by addition of an appropriate amount of solutes because the number of active bubbles increases [86, 87]. It has also been experimentally confirmed that bubble size is smaller in an aqueous surfactant solution compared to that in pure water in acoustic cavitation [88].

2.18 Bubble–Bubble Interaction

As discussed in Sect. 2.16, a pulsating bubble radiates an acoustic wave into surrounding liquid according to Eq. (2.101).

$$p = \frac{\rho}{r}\left(2R\dot{R}^2 + R^2\ddot{R}\right) \tag{2.104}$$

where p is the acoustic pressure radiated from a bubble, ρ is the liquid density, and r is the distance from a radiating bubble. The influence of an acoustic wave radiated by the surrounding bubbles on bubble pulsation is called *bubble–bubble interaction* (Fig. 2.35) [33]. The effect is taken into account in the Keller equation (Eq. 2.31) simply by using the following $p_s(t)$.

$$p_s(t) = -A\,\sin\omega t + \rho\sum_i \frac{1}{r_i}\left(2R_i\dot{R}_i^2 + R_i^2\ddot{R}_i\right) \tag{2.105}$$

where r_i is the distance from the bubble numbered i, R_i is the instantaneous radius of bubble numbered i, and summation is for all the surrounding bubbles. By neglecting terms of order $(R_i/r_i)\left(\dot{R}_j/c_\infty\right)$, the following equation is obtained from the Keller equation [75].

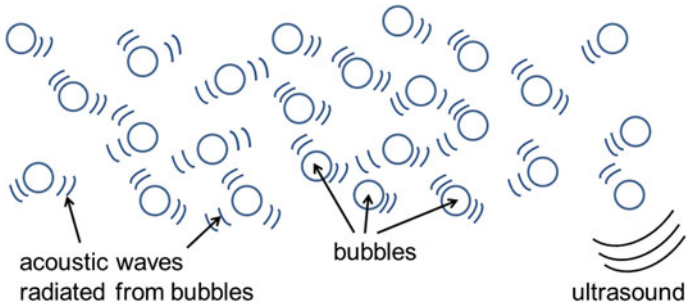

Fig. 2.35 Bubble–bubble interaction. Pulsation of a bubble is influenced by the acoustic waves radiated by the surrounding bubbles. Reprinted with permission from Yasui [33]. Copyright (2016), Springer

$$\left(1-\frac{\dot{R}}{c_\infty}\right)R\ddot{R}+\frac{3}{2}\dot{R}^2\left(1-\frac{\dot{R}}{3c_\infty}\right)=\frac{1}{\rho_{\mathrm{L},\infty}}\left(1+\frac{\dot{R}}{c_\infty}\right)(p_\mathrm{B}+A\,\sin\omega t-p_\infty)+\frac{R}{c_\infty\rho_{\mathrm{L},\infty}}\frac{\mathrm{d}p_\mathrm{B}}{\mathrm{d}t}-\sum_i\frac{1}{r_i}\left(2R_i\dot{R}_i^2+R_i^2\ddot{R}_i\right) \tag{2.106}$$

In order to numerically solve Eq. (2.106), the number of equations necessary to simultaneously solve is equivalent to the number of bubbles. However, it is computationally expensive. Thus, the number of equations is dramatically reduced to 1 by assuming that the radius of each bubble is the same for all the bubbles. Furthermore, the spatial distribution of the bubbles is assumed to be uniform. Under this homogeneous bubble approximation, a set of Eqs. (2.106) is reduced to a single Eq. (2.107) [74, 89–91].

$$\left(1-\frac{\dot{R}}{c_\infty}\right)R\ddot{R}+\frac{3}{2}\dot{R}^2\left(1-\frac{\dot{R}}{3c_\infty}\right)=\frac{1}{\rho_{\mathrm{L},\infty}}\left(1+\frac{\dot{R}}{c_\infty}\right)(p_\mathrm{B}+A\,\sin\omega t-p_\infty)+\frac{R}{c_\infty\rho_{\mathrm{L},\infty}}\frac{\mathrm{d}p_\mathrm{B}}{\mathrm{d}t}-S\left(2R\dot{R}^2+R^2\ddot{R}\right) \tag{2.107}$$

where

$$S=\sum_i\frac{1}{r_i}=\int_{l_\mathrm{min}}^{l_\mathrm{max}}\frac{4\pi r^2 n}{r}\,\mathrm{d}r=2\pi n\left(l_\mathrm{max}^2-l_\mathrm{min}^2\right)\approx 2\pi n l_\mathrm{max}^2 \tag{2.108}$$

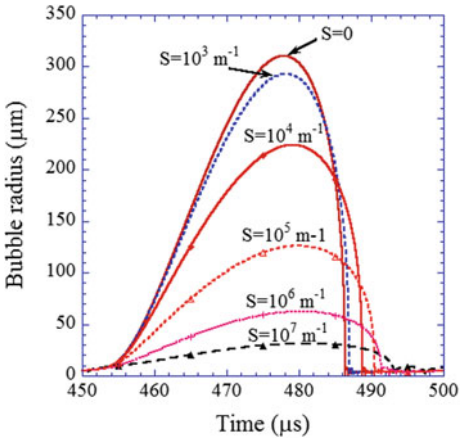

Fig. 2.36 Results of the numerical simulations on radius–time curves for various coupling strengths (S) of bubble–bubble interaction. The frequency and pressure amplitude of ultrasound are 20 kHz and 10 bar, respectively. The ambient static pressure is 5 atm. The ambient bubble radius is 5 μm. The liquid viscosity is 1 mPa s. Reprinted with permission from Yasui et al. [90]. Copyright (2011), AIP Publishing LLC

where $l_{\max}$ is the radius of a bubble cloud, $l_{\min}$ is the distance between a bubble and a nearest bubble, $l_{\max} \gg l_{\min}$ is assumed in the last equation, and n is the number density of the bubbles. The factor S is called the *coupling strength of bubble–bubble interaction* [74, 89–92]. The results of several numerical simulations of Eq. (2.107) have shown that bubble expansion is more strongly suppressed as the coupling strength increases (Fig. 2.36) [90].

Following the method described in Sect. 2.12, the resonance angular frequency of a bubble is derived from Eq. (2.107) as follows [89].

$$\omega_0 = \sqrt{\frac{3\gamma p_\infty + (3\gamma - 1)2\sigma/R_0}{\rho_{\mathrm{L},\infty} R_0 \left(R_0 + SR_0^2 + 4\mu/c_\infty \rho_{\mathrm{L},\infty}\right)}} \tag{2.109}$$

Thus, the resonance frequency of a bubble considerably decreases as the coupling strength (S) increases above about 10^5 m^{-1} [89].

2.19 Acoustic Cavitation Noise

In experiments of acoustic cavitation, acoustic noise from cavitating liquid is often heard especially at relatively low driving ultrasonic frequencies. Such noise is called *acoustic cavitation noise*. From experimental measurement of acoustic emission originating from a single bubble in SBSL, most of the acoustic emissions from a pulsating bubble occur at the end of a violent bubble collapse (Fig. 2.37)

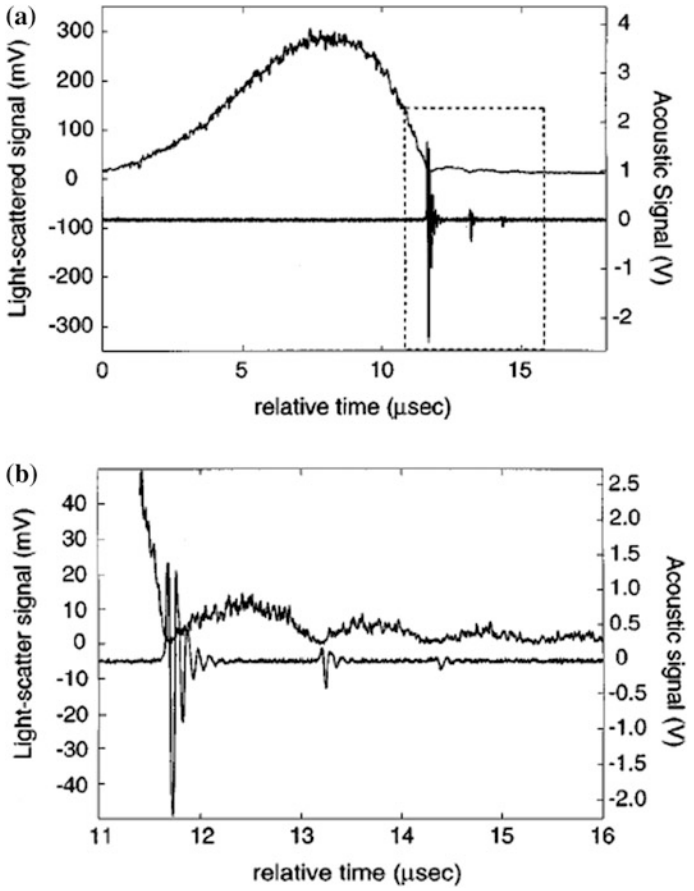

Fig. 2.37 Radius–time curve measured by light scattering and acoustic signal measured with a hydrophone for a single bubble in SBSL experiment. The ultrasonic frequency was 33.8 kHz. **a** For about 18 μs. **b** A detailed view of the boxed area in (**a**). Reprinted with permission from Matula et al. [93]. Copyright (1998), AIP Publishing LLC

[93]. In other words, most of acoustic cavitation noise originates in shock waves emitted from acoustic cavitation bubbles (Sect. 2.13).

According to Eq. (2.105), acoustic pressure (P) radiated from pulsating bubbles is given as follows.

$$P = \rho \sum_i \frac{1}{r_i} \left(2R_i \dot{R}_i^2 + R_i^2 \ddot{R}_i\right) = S\rho\left(R^2 \ddot{R} + 2R\dot{R}^2\right) \tag{2.110}$$

where the homogeneous bubble approximation is used in the last equation. When some of bubbles disintegrate into "daughter" bubbles by shape instability, the

coupling strength (S) in Eq. (2.110) changes with time due to a change in number density of bubbles [94].

Shape instability of a bubble is numerically simulated as follows [38, 94, 95]. The amplitude of non-spherical component of bubble shapes is numerically calculated for this purpose. A small distortion of the spherical surface of a bubble is described by $R(t) + a_n(t)Y_n$, where $R(t)$ is the instantaneous mean radius of a bubble at time t, Y_n is a spherical harmonic of degree n, and $a_n(t)$ is the amplitude of non-spherical component. The dynamics for the amplitude of the non-spherical component $a_n(t)$ is given as follows [95].

$$\ddot{a}_n + B_n(t)\dot{a}_n - A_n(t)a_n = 0 \tag{2.111}$$

where [dot] denotes time derivative such as $\ddot{a}_n = \frac{\mathrm{d}^2 a_n}{\mathrm{d}t^2}$ and $\dot{a}_n = \frac{\mathrm{d}a_n}{\mathrm{d}t}$, and the coefficients $A_n(t)$ and $B_n(t)$ are given as follows [95].

$$A_n(t) = (n-1)\frac{\ddot{R}}{R} - \frac{\beta_n \sigma}{\rho R^3} - \left[(n-1)(n+2) + 2n(n+2)(n-1)\frac{\delta}{R}\right]\frac{2\mu\dot{R}}{R^3} \tag{2.112}$$

$$B_n(t) = \frac{3\dot{R}}{R} + \left[(n+2)(2n+1) - 2n(n+2)^2\frac{\delta}{R}\right]\frac{2\mu}{R^2} \tag{2.113}$$

where $\beta_n = (n-1)(n+1)(n+2)$, σ is surface tension, μ is liquid viscosity, and δ is thickness of thin layer where fluid flows.

$$\delta = \min\left(\sqrt{\frac{\mu}{\omega}}, \frac{R}{2n}\right) \tag{2.114}$$

where min means the minimum value in the two quantities in the brackets, and ω is angular frequency of ultrasound. When $a_n(t)$ becomes larger than $R(t)$, then a bubble is considered to be disintegrated into "daughter" bubbles by the shape instability [95].

In actual experiments, the acoustic cavitation noise is measured with a hydrophone. A hydrophone has a cutoff frequency, and its response is approximately modeled using the following equation [94, 96].

$$\ddot{U} + 2\gamma_{\mathrm{dh}}\pi f_{\mathrm{c}}\dot{U} + 4\pi^2 f_{\mathrm{c}}^2 U = P(t) - A\,\sin\omega t \tag{2.115}$$

where U is the hydrophone signal, γ_{dh} is the coefficient for damping, f_{c} is the characteristic frequency of hydrophone, $P(t)$ is the acoustic pressure radiated from pulsating bubbles given by Eq. (2.110), and $-A\,\sin\omega t$ is the acoustic pressure of the driving ultrasound. The characteristic frequency (f_{c}) of the hydrophone is related to the cutoff frequency since the sensitivity of hydrophone above f_{c} is lower than that below f_{c}. For a larger value of f_{c}, the intensity of the high-frequency component becomes stronger. For a larger value of γ_{dh}, the frequency cutoff becomes sharper.

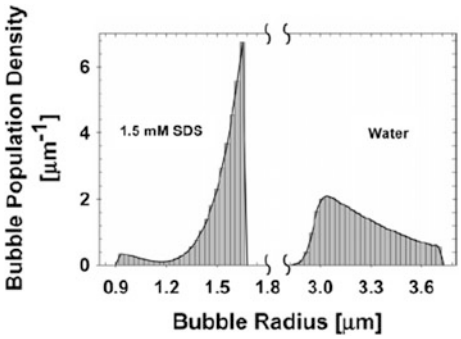

Fig. 2.38 Bubble population density versus the bubble radius for water and 1.5 mM SDS solution, estimated from the experimental data on quenching of SL intensity by increasing pulse-off time of pulsed ultrasound (515 kHz). Reprinted with permission from Lee et al. [88]. Copyright (2005), American Chemical Society

The frequency spectra of the acoustic cavitation noise measured with a hydrophone consist of the strongest peak at a driving ultrasonic frequency (515 kHz) (fundamental frequency), discrete peaks at integer multiple of the fundamental frequency (harmonics), discrete weaker peaks at a half of the fundamental frequency (subharmonic) and its integer multiple (ultra-harmonics), and weaker broadband continuum component (broadband noise) [97]. Surprisingly, the frequency spectra from low-concentration surfactant (sodium dodecyl sulfate, SDS) solution in the concentration range of 0.5–2 mM consist of only discrete peaks at fundamental frequency and its integer multiple [97]. The broadband component is significantly weaker than that in pure water. As already pointed out in Sect. 2.17, the bubble size is smaller in aqueous surfactant solution than that in pure water in a certain concentration range. For example, the bubble radii in 1.5 mM SDS aqueous solution were in the range of 0.9–1.7 μm, while those in pure water were in the range of 2.8–3.7 μm, which were experimentally measured from quenching of sonoluminescence intensity by increasing pulse-off time in pulsed ultrasound at 515 kHz (Fig. 2.38) [88].

According to the numerical simulations of amplitude of non-spherical component of bubble shape (Eq. 2.111) using the modified Keller equation (Eq. 2.107), a bubble is shape stable when the ambient bubble radius is 1.5 μm which is typical in a 1.5 mM SDS solution [94]. Thus, in this case, there is no temporal variation in the number of bubbles and the coupling strength. The bubble pulsation is temporally periodic (Fig. 2.39a), and the acoustic emission is also temporally periodic because there is no temporal variation in the number of bubbles (Fig. 2.39b) [94]. Accordingly, the hydrophone signal simulated using Eq. (2.115) is also temporally periodic (Fig. 2.39c). Then, the frequency spectrum of the hydrophone signal only consists of fundamental frequency (515 kHz) and its harmonics (Fig. 2.39d). It is consistent with the experimental measurement [97]. Even with strong shock waves emitted from bubbles (Fig. 2.39b), there is no broadband component in the acoustic

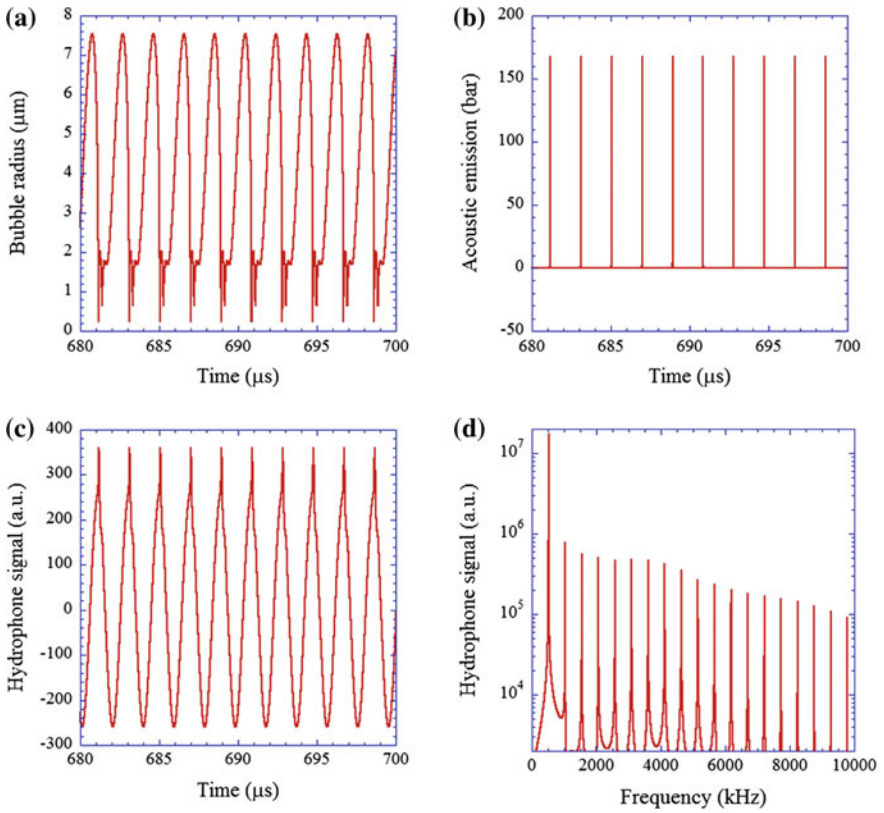

Fig. 2.39 Results from numerical simulations with a constant coupling strength of 10^4 m^{-1} (without a temporal fluctuation in the number of bubbles). The ambient bubble radius is 1.5 μm, which is typical in low-concentration SDS solutions. The frequency and pressure amplitude of ultrasound are 515 kHz and 2.6 bar, respectively. **a** Bubble radius. **b** Acoustic pressure radiated from bubbles (Eq. 2.110). **c** Hydrophone signal (Eq. 2.115). **d** Frequency spectrum of the hydrophone signal. Reprinted with permission from Yasui et al. [94]. Copyright (2010), Elsevier

cavitation spectrum. In other words, broadband noise is not solely originated in shock wave emissions.

In the case of ambient radius of 3 μm which is typical in pure water at 515 kHz, a bubble disintegrates into "daughter" bubbles in four (4) acoustic cycles [94]. Thus, in this case, there is a temporal fluctuation in the number of bubbles as well as the coupling strength. Even with this temporal variation, the radius–time curve is almost temporally periodic (Fig. 2.40a). However, the peaks in acoustic pressure due to shock wave emissions temporally fluctuate according to the temporal fluctuation in number of bubbles (Fig. 2.40b). As a result, small peaks in hydrophone signal caused by the shock waves also temporally fluctuate (Fig. 2.40c). Then, there is a strong broadband component in the frequency spectrum of the hydrophone signal (Fig. 2.40d) [94]. Thus, the origin of the broadband noise is temporal

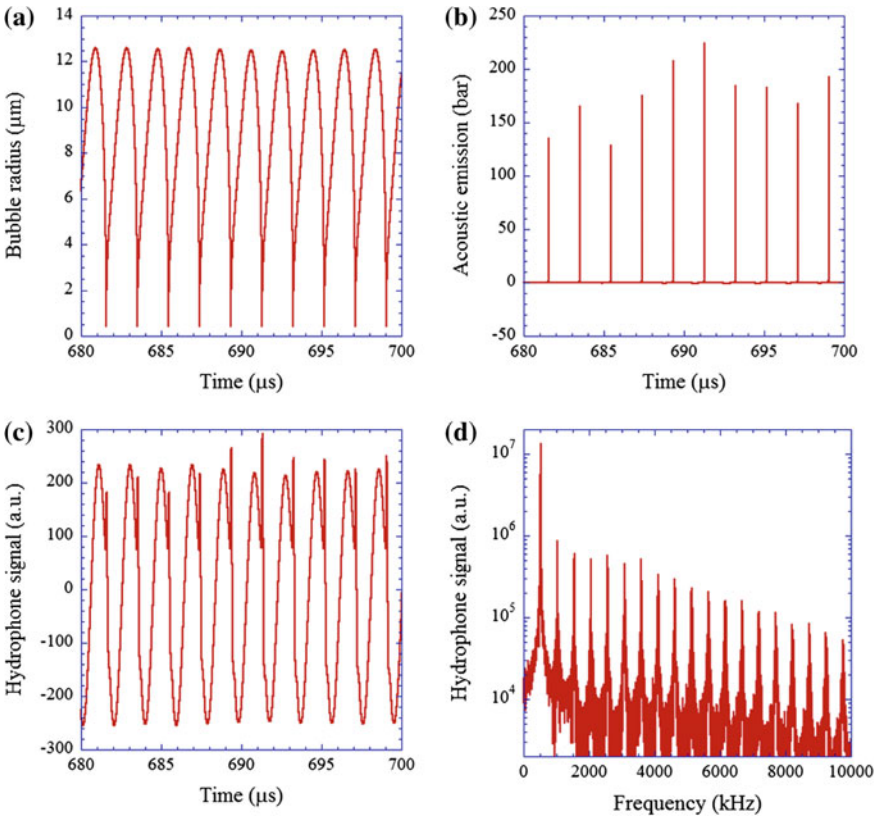

Fig. 2.40 Results from numerical simulations with a temporal fluctuation in the number of bubbles (coupling strength). The ambient bubble radius is 3 μm, which is typical in pure water. The frequency and pressure amplitude of ultrasound are the same as those shown in Fig. 2.39. **a** Bubble radius. **b** Acoustic pressure radiated from bubbles (Eq. 2.110). **c** Hydrophone signal (Eq. 2.115). **d** Frequency spectrum of the hydrophone signal. Reprinted with permission from Yasui et al. [94]. Copyright (2010), Elsevier

fluctuation in the number of bubbles. Broadband noise also results from non-periodic chaotic pulsation of bubbles as well as from initial transient pulsation of bubbles before reaching steady-state pulsation [94]. However, the contribution to the actual broadband noise is minor at least under the experimental condition of Ref. [97].

Subharmonic and ultra-harmonic originate from periodic bubble pulsation with doubled acoustic period of larger bubbles with ambient radius of 5 μm under this condition [94]. When the number of bubbles is much larger and the coupling strength is much larger, broadband noise as well as sub- and ultra-harmonics is also resulted from the bubble–bubble interaction [the last term in Eq. (2.107)] [94]. Further studies are required on the origin of the broadband noise [98].

2.20 Acoustic Streaming and Microstreaming

A fluid (liquid) parcel moves forward and backward due to acoustic wave propagation. The periodic motion is exactly symmetric under "ideal" conditions, and a fluid parcel returns to the same position after one acoustic cycle. However, under real situations, a fluid parcel does not return to the same position after one acoustic cycle. In other words, there is some DC (direct current) fluid flow associated with the acoustic wave propagation. Such DC fluid flow is called *acoustic streaming* [99–101].

There are mainly two types of acoustic streaming. One is accelerating DC fluid flow in the direction of the acoustic traveling wave propagation. This is caused by the attenuation of an acoustic traveling wave (ultrasound). In many cases, the attenuation is due to the viscosity of the fluid (liquid). Due to attenuation, the radiation pressure pushing a fluid parcel becomes stronger than that pulling it. This unbalance of radiation pressure causes the accelerating fluid flow which is called *Eckert streaming*. The other type is a vortex-like streaming caused by viscous stress at the boundary layer near a wall or an object irrespective of the situation of a traveling or standing wave, which is called *Rayleigh streaming*. When the length scale for streaming caused by viscous stress near an object such as a bubble is much less than the acoustic wavelength, it is called *microstreaming*.

Microstreaming occurs not only around a bubble but also around a solid particle. However, it is much more significant around a bubble because the speed of microstreaming is proportional to the square of vibration speed of an object. The speed of microstreaming around a pulsating bubble is 10^2–10^6 times larger than that around a solid particle because it is on the order of $U^2/\omega a$, where U is the vibration speed of an object, ω is the angular frequency of an acoustic wave (ultrasound), and a is radius of an object [102]. Thus, the term "microstreaming" is usually used for liquid streaming around a pulsating bubble. In Fig. 2.41, some examples of pattern of microstreaming around a pulsating bubble on a solid surface are shown [103].

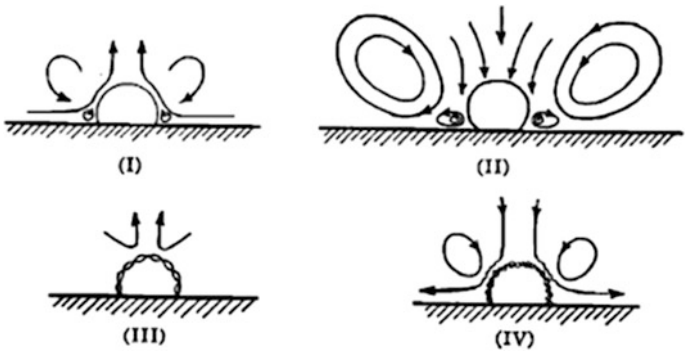

Fig. 2.41 Four types of microstreaming around a pulsating bubble. Reprinted with permission from Elder [103]. Copyright (1959), AIP Publishing LLC

Liquid flow associated with acoustic cavitation is highly complex. Ultrasound is strongly attenuated by cavitation bubbles, which intensifies Eckert streaming. Bubbles move due to primary and secondary Bjerknes forces, and liquid flow is influenced by the drag forces of bubbles. There is also microstreaming around pulsating bubbles. Rayleigh streaming also occurs near a wall. Liquid flow associated with acoustic cavitation is not fully understood at present [104].

References

1. Atkins P, de Paula J (2010) Atkins' physical chemistry, 9th edn. Oxford University Press, Oxford
2. Yasui K (2015) Dynamics of acoustic bubbles. In: Grieser F, Choi PK, Enomoto N, Harada H, Okitsu K, Yasui K (eds) Sonochemistry and the acoustic bubble. Elsevier, Amsterdam
3. Yasui K (2016) Mechanism for stability of ultrafine bubbles. Jpn J Multiph Flow 30:19–26 (in Japanese)
4. Keller JB, Miksis M (1980) Bubble oscillations of large amplitude. J Acoust Soc Am 68:628–633. doi:10.1121/1.384720
5. Prosperetti A, Lezzi A (1986) Bubble dynamics in a compressible liquid. Part 1. First-order theory. J Fluid Mech 168:457–478. doi:10.1017/S0022112086000460
6. Yasui K (1996) Variation of liquid temperature at bubble wall near the sonoluminescence threshold. J Phys Soc Jpn 65:2830–2840. doi:10.1143/JPSJ.65.2830
7. Pozrikidis C (2017) Fluid dynamics, 3rd edn. Springer, New York
8. Storey BD, Szeri AJ (1999) Mixture segregation within sonoluminescence bubbles. J Fluid Mech 396:203–221. doi:10.1017/S0022112099005984
9. Yasui K (2001) Effect of liquid temperature on sonoluminescence. Phys Rev E 64:016310. doi:10.1103/PhysRevE.64.016310
10. Kundu PK (1990) Fluid mechanics. Academic Press, San Diego
11. Akhatov I, Lindau O, Topolnikov A, Mettin R, Vakhitova N, Lauterborn W (2001) Collapse and rebound of a laser-induced cavitation bubble. Phys Fluids 13:2805–2819. doi:10.1063/1.1401810
12. Muller S, Bachmann M, Kroninger D, Kurz T, Helluy P (2009) Comparison and validation of compressible flow simulations of laser-induced cavitation bubbles. Comput Fluid 38:1850–1862. doi:10.1016/j.compfluid.2009.04.004
13. Gould H, Tobochnik J, Christian W (2007) An introduction to computer simulation methods, applications to physical systems, 3rd edn. Pearson, Addison Wesley, San Francisco
14. Yasui K (1997) Alternative model of single-bubble sonoluminescence. Phys Rev E 56:6750–6760. doi:10.1103/PhysRevE.56.6750
15. Yasui K (1996) A new formulation of bubble dynamics for sonoluminescence. Ph.D. thesis, Waseda University, Japan
16. Yasui K, Tuziuti T, Kanematsu W (2016) Extreme conditions in a dissolving air nanobubble. Phys Rev E 94:013106. doi:10.1103/PhysREvE.94.013106
17. Yasui K, Tuziuti T, Sivakumar M, Iida Y (2005) Theoretical study of single-bubble sonochemistry. J Chem Phys 122:224706. doi:10.1063/1.1925607
18. Toegel R, Lohse D (2003) Phase diagrams for sonoluminescing bubbles: a comparison between experiment and theory. J Chem Phys 118:1863–1875. doi:10.1063/1.1531610
19. Storey BD, Szeri AJ (2001) A reduced model of cavitation physics for use in sonochemistry. Proc R Soc Lond A 457:1685–1700. doi:10.1098/rspa.2001.0784

20. Lohse D, Brenner MP, Dupont TF, Hilgenfeldt S, Johnston B (1997) Sonoluminescing air bubbles rectify argon. Phys Rev Lett 78:1359–1362. doi:10.1103/PhysRevLett.78.1359
21. Brenner MP, Hilgenfeldt S, Lohse D (2002) Single-bubble sonoluminescence. Rev Mod Phys 74:425–484. doi:10.1103/RevModPhys.74.425
22. Yasui K, Tuziuti T, Sivakumar M, Iida Y (2004) Sonoluminescence. Appl Spectrosc Rev 39:399–436. doi:10.1081/ASR-200030202
23. Storey BD, Szeri AJ (2000) Water vapour, sonoluminescence and sonochemistry. Proc R Soc Lond A 456:1685–1709. doi:10.1098/rspa.2000.0582
24. Yasui K (2001) Single-bubble sonoluminescence from noble gases. Phys Rev E 63:035301. doi:10.1103/PhysRevE.63.035301
25. Yasui K (2002) Segregation of vapor and gas in a sonoluminescing bubble. Ultrasonics 40:643–647. doi:10.1016/S0041-624X(02)00190-7
26. Schrage RW (1953) A theoretical study of interphase mass transfer. Columbia University Press, New York
27. Fujikawa S, Akamatsu T (1980) Effects of the no-equilibrium condensation of vapour on the pressure wave produced by the collapse of a bubble in a liquid. J Fluid Mech 97:481–512. doi:10.1017/S0022112080002662
28. Matsumoto M (1996) Molecular dynamics simulation of interphase transport at liquid surfaces. Fluid Phase Equilib 125:195–203. doi:10.1016/S0378-3812(96)03123-8
29. Yasui K (1998) Effect of non-equilibrium evaporation and condensation on bubble dynamics near the sonoluminescence threshold. Ultrasonics 36:575–580. doi:10.1016/S0041-6244(97)00107-8
30. Suslick KS, Hammerton DA, Cline RE Jr (1986) The sonochemical hot spot. J Am Chem Soc 108:5641–5642. doi:10.1021/ja00278a055
31. Hua I, Hochemer RH, Hoffmann MR (1995) Sonolytic hydrolysis of p-nitrophenyl acetate: the role of supercritical water. J Phys Chem 99:2335–2342. doi:10.1021/j100008a015
32. Moriwaki H, Takagi Y, Tanaka M, Tsuruho K, Okitsu K, Maeda Y (2005) Sonochemical decomposition of perfluorooctane sulfonate and perfluorooctanoic acid. Environ Sci Technol 39:3388–3392. doi:10.1021/es040342v
33. Yasui K (2016) Unsolved problems in acoustic cavitation. In: Ashokkumar M, Cavalieri F, Chemat F, Okitsu K, Sambandam A, Yasui K, Zisu B (eds) Handbook of ultrasonics and sonochemistry. Springer, Singapore
34. Vuong VQ, Szeri AJ (1996) Sonoluminescence and diffusive transport. Phys Fluids 8:2354–2364. doi:10.1063/1.869020
35. Kamath V, Prosperetti A, Egolfopoulos FN (1993) A theoretical study of sonoluminescence. J Acoust Soc Am 94:248–260. doi:10.1121/1.407083
36. Shen Y, Yasui K, Sun Z, Mei B, You M, Zhu T (2016) Study on the spatial distribution of the liquid temperature near a cavitation bubble wall. Ultrason Sonochem 29:394–400. doi:10.1016/j.ultsonch.2015.10.015
37. Eller A, Flynn HG (1965) Rectified diffusion during nonlinear pulsations of cavitation bubbles. J Acoust Soc Am 37:493–503. doi:10.1121/1.1909357
38. Yasui K (2002) Influence of ultrasonic frequency on multibubble sonoluminescence. J Acoust Soc Am 112:1405–1413. doi:10.1121/1.1502898
39. Leighton TG (1994) The acoustic bubble. Academic Press, London
40. Leong T, Ashokkumar M, Kentish S (2016) The growth of bubbles in an acoustic field by rectified diffusion. In: Ashokkumar M, Cavalieri F, Chemat F, Okitsu K, Sambandam A, Yasui K, Zisu B (eds) Handbook of ultrasonics and sonochemistry. Springer, Singapore
41. Crum LA (1980) Measurements of the growth of air bubbles by rectified diffusion. J Acoust Soc Am 68:203–211. doi:10.1121/1.384624
42. Louisnard O, Gomez F (2003) Growth by rectified diffusion of strongly acoustically forced gas bubbles in nearly saturated liquids. Phys Rev E 67:036610. doi:10.1103/PhysRevE.67.036610

43. Yasui K, Tuziuti T, Lee J, Kozuka T, Towata A, Iida Y (2008) The range of ambient radius for an active bubble in sonoluminescence and sonochemical reactions. J Chem Phys 128:184705. doi:10.1063/1.2919119
44. Yasui K (1997) Chemical reactions in a sonoluminescing bubble. J Phys Soc Jpn 66:2911–2920. doi:10.1143/JPSJ.66.2911
45. Yasui K, Tuziuti T, Iida Y, Mitome H (2003) Theoretical study of the ambient-pressure dependence of sonochemical reactions. J Chem Phys 119:346–356. doi:10.1063/1.1576375
46. Didenko YT, Suslick KS (2002) The energy efficiency of formation of phtons, radicals and ions during single-bubble cavitation. Nature (London) 418:394–397. doi:10.1038/nature00895
47. Matula TJ, Crum LA (1998) Evidence for gas exchange in single-bubble sonoluminescence. Phys Rev Lett 80:865–868. doi:10.1103/PhysRevLett.80.865
48. Yasui K, Tuziuti T, Kozuka T, Towata A, Iida Y (2007) Relationship between the bubble temperature and main oxidant created inside an air bubble under ultrasound. J Chem Phys 127:154502. doi:10.1063/1.2790420
49. Yasui K, Tuziuti T, Iida Y (2004) Optimum bubble temperature for the sonochemical production of oxidants. Ultrasonics 42:579–584. doi:10.1016/j.ultras.2003.12.005
50. Hart EJ, Henglein A (1985) Free radical and free atom reactions in the sonolysis of aqueous iodide and formate solutions. J Phys Chem 89:4342–4347. doi:10.1021/j100266a038
51. Yasui K (2002) Effect of volatile solutes on sonoluminescence. J Chem Phys 116:2945–2954. doi:10.1063/1.1436122
52. Ashokkumar M, Crum LA, Frensley CA, Grieser F, Matula TJ, McNamara WB III, Suslick KS (2000) Effect of solutes on single-bubble sonoluminescence in water. J Phys Chem 104:8462–8465. doi:10.1021/jp000463r
53. Guan J, Matula TJ (2003) Time scales for quenching single-bubble sonoluminescence in the presence of alcohols. J Phys Chem B 107:8917–8921. doi:10.1021/jp026494z
54. Kinsler LE, Frey AR, Coppens AB, Sanders JV (1982) Fundamentals of acoustics, 3rd edn. Wiley, New York
55. Landau LD, Lifshitz EM (1987) Fluid mechanics, 2nd edn. (trans: Sykes JB, Reid WH). Elsevier, Amsterdam
56. Holzfuss J, Ruggeberg M, Billo A (1998) Shock wave emissions of a sonoluminescing bubble. Phys Rev Lett 81:5434–5437. doi:10.1103/PhysRevLett.81.5434
57. Hickling R, Plesset MS (1964) Collapse and rebound of a spherical bubble in water. Phys Fluids 7:7–14. doi:10.1063/1.1711058
58. Wu CC, Roberts PH (1993) Shock-wave propagation in a sonoluminescing gas bubble. Phys Rev Lett 70:3424–3427. doi:10.1103/PhysRevLett.70.3424
59. Moss WC, Clarke DB, White JW, Young DA (1994) Hydrodynamic simulations of bubble collapse and picosecond sonoluminescence. Phys Fluids 6:2979–2985. doi:10.1063/1.868124
60. Nigmatulin RI, Akhatov IS, Topolnikov AS, Bolotnova RK, Vakhitova NK, Lahey RT Jr, Taleyarkhan RP (2005) Theory of supercompression of vapor bubbles and nanoscale thermonuclear fusion. Phys Fluids 17:107106. doi:10.1063/1.2104556
61. Yuan L, Cheng HY, Chu MC, Leung PT (1998) Physical parameters affecting sonoluminescence: a self-consistent hydrodynamic study. Phys Rev E 57:4265–4280. doi:10.1103/PhysRevE.57.4265
62. Cheng HY, Chu MC, Leung PT, Yuan L (1998) How important are shock waves to single-bubble sonoluminescence? Phys Rev E 58:R2705–R2708. doi:10.1103/PhysRevE.58.R2705
63. Yuan L (2005) Sonochemical effects on single-bubble sonoluminescence. Phys Rev E 72:046309. doi:10.1103/PhysRevE.72.046309
64. An Y (2006) Mechanism of single-bubble sonoluminescence. Phys Rev E 74:026304. doi:10.1103/PhysRevE.74.026304
65. An Y, Li C (2008) Spectral lines of OH radicals and Na atoms in sonoluminescence. Phys Rev E 78:046313. doi:10.1103/PhysRevE.78.046313

66. Vuong VQ, Szeri AJ, Young DA (1999) Shock formation within sonoluminescence bubbles. Phys Fluids 11:10–17. doi:10.1063/1.869920
67. Ohl CD, Arora M, Dijkink R, Janve V, Lohse D (2006) Surface cleaning from laser-induced cavitation bubbles. Appl Phys Lett 89:074102. doi:10.1063/1.2337506
68. Plesset MS, Chapman RB (1971) Collapse of an initially spherical vapour cavity in the neighbourhood of a solid boundary. J Fluid Mech 47:283–290. doi:10.1017/S0022112071001058
69. Lamminen MO, Walker HW, Weavers LK (2004) Mechanism and factors influencing the ultrasonic cleaning of particle-fouled ceramic membranes. J Membr Sci 237:213–223. doi:10.1016/j.memsci.2004.02.031
70. Bremond N, Arora M, Dammer SM, Lohse D (2006) Interaction of cavitation bubbles on a wall. Phys Fluids 18:121505. doi:10.1063/1.2396922
71. Calvisi ML, Lindau O, Blake JR, Szeri AJ (2007) Shape stability and violent collapse of microbubbles in acoustic traveling waves. Phys Fluids 19:047101. doi:10.1063/1.2716633
72. Mettin R (2005) Bubble structures in acoustic cavitation. In: Doinikov AA (ed) Bubble and particle dynamics in acoustic fields: modern trends and applications. Research Signpost, Trivandrum
73. Matula TJ, Cordry SM, Roy RA, Crum LA (1997) Bjerknes force and bubble levitation under single-bubble sonoluminescence conditions. J Acoust Soc Am 102:1522–1527. doi:10.1121/1.420065
74. Yasui K, Iida Y, Tuziuti T, Kozuka T, Towata A (2008) Strongly interacting bubbles under an ultrasonic horn. Phys Rev E 77:016609. doi:10.1103/PhysRevE.77.016609
75. Mettin R, Akhatov I, Parlitz U, Ohl CD, Lauterborn W (1997) Bjerknes forces between small cavitation bubbles in a strong acoustic field. Phys Rev E 56:2924–2931. doi:10.1103/PhysRevE.56.2924
76. Firouzi M, Howes T, Nguyen AV (2015) A quantitative review of the transition salt concentration for inhibiting bubble coalescence. Adv Colloid Interface Sci 222:305–318. doi:10.1016/j.cis.2014.07.005
77. Prince MJ, Blanch HW (1990) Transition electrolyte concentrations for bubble coalescence. AIChE J 36:1425–1429. doi:10.1002/aic.690360915
78. Prince MJ, Blanch HW (1990) Bubble coalescence and break-up in air-sparged bubble columns. AIChE J 36:1485–1499. doi:10.1002/aic.690361004
79. Craig VSJ, Ninham BW, Pashley RM (1993) Effect of electrolytes on bubble coalescence. Nature (London) 364:317–319. doi:10.1038/364317a0
80. Christenson HK, Yaminsky VV (1995) Solute effects on bubble coalescence. J Phys Chem 99:10420. doi:10.1021/j100025a052
81. Oolman TO, Blanch HW (1986) Bubble coalescence in stagnant liquids. Chem Eng Commun 43:237–261. doi:10.1080/00986448608911334
82. Lee JC, Meyrick DL (1970) Gas-liquid interfacial areas in salt solutions in an agitated tank. Trans Inst Chem Eng 48:T37–T45
83. Marrucci G (1969) A theory of coalescence. Chem Eng Sci 24:975–985. doi:10.1016/0009-2509(69)87006-5
84. Iida Y, Ashokkumar M, Tuziuti T, Kozuka T, Yasui K, Towata A, Lee J (2010) Bubble population phenomena in sonochemical reactor: I estimation of bubble size distribution and its number density with pulsed sonication—laser diffraction method. Ultrason Sonochem 17:473–479. doi:10.1016/j.ultsonch.2009.08.018
85. Iida Y, Ashokkumar M, Tuziuti T, Kozuka T, Yasui K, Towata A, Lee J (2010) Bubble population phenomena in sonochemical reactor: II. Estimation of bubble size distribution and its number density by simple coalescence model calculation. Ultrason Sonochem 17:480–486. doi:10.1016/j.ultsonch.2009.08.017
86. Ashokkumar M, Hall R, Mulvaney P, Grieser F (1997) Sonoluminescence from aqueous alcohol and surfactant solutions. J Phys Chem 101:10845–10850. doi:10.1021/jp972477b

87. Sunartio D, Ashokkumar M, Grieser F (2005) The influence of acoustic power on multibubble sonoluminescence in aqueous solution containing organic solutes. J Phys Chem B 109:20044–20050. doi:10.1021/jp052747n
88. Lee J, Ashokkumar M, Kentish S, Grieser F (2005) Determination of the size distribution of sonoluminescence bubbles in a pulsed acoustic field. J Am Chem Soc 127:16810–16811. doi:10.1021/ja0566432
89. Yasui K, Lee J, Tuziuti T, Towata A, Kozuka T, Iida Y (2009) Influence of the bubble-bubble interaction on destruction of encapsulated microbubbles under ultrasound. J Acoust Soc Am 126:973–982. doi:10.1121/1.3179677
90. Yasui K, Towata A, Tuziuti T, Kozuka T, Kato K (2011) Effect of static pressure on acoustic energy radiated by cavitation bubbles in viscous liquids under ultrasound. J Acoust Soc Am 130:3233–3242. doi:10.1121/1.3626130
91. Yasui K, Kato K (2012) Bubble dynamics and sonoluminescence from helium or xenon in mercury and water. Phys Rev E 86:036320. doi:10.1103/PhysRevE.86.036320. Erratum. Phys Rev E 86:069901. doi:10.1103/PhysRevE.86.069901
92. Guedra M, Cornu C, Inserra C (2017) A derivation of the stable cavitation threshold accounting for bubble-bubble interactions. Ultrason Sonochem 38:168–173. doi:10.1016/j.ultsonch.2017.03.010
93. Matula TJ, Hallaj IM, Cleveland RO, Crum LA, Moss WC, Roy RA (1998) The acoustic emissions from single-bubble sonoluminescence. J Acoust Soc Am 103:1377–1382. doi:10.1121/1.421279
94. Yasui K, Tuziuti T, Lee J, Kozuka T, Towata A, Iida Y (2010) Numerical simulations of acoustic cavitation noise with the temporal fluctuation in the number of bubbles. Ultrason Sonochem 17:460–472. doi:10.1016/j.ultsonch.2009.08.014
95. Hilgenfeldt S, Lohse D, Brenner MP (1996) Phase diagrams for sonoluminescing bubbles. Phys Fluids 8:2808–2826. doi:10.1063/1.869131
96. Luther S, Sushchik M, Parlitz U, Akhatov I, Lauterborn W (2000) Is cavitation noise governed by a low-dimensional chaotic attractor? AIP Conf Proc 524:355–358
97. Ashokkumar M, Hodnett M, Zeqiri B, Grieser F, Price GJ (2007) Acoustic emission spectra from 515 kHz cavitation in aqueous solutions containing surface-active solutes. J Am Chem Soc 129:2250–2258. doi:10.1021/ja067960r
98. Lauterborn W, Mettin R (2015) Acoustic cavitation: bubble dynamics in high-power ultrasonic fields. In: Gallego-Juarez JA, Graff KF (eds) Power ultrasonics—applications of high-intensity ultrasound. Woodhead Publishing, Cambridge (Elsevier, Amsterdam)
99. Manasseh R (2016) Acoustic bubbles, acoustic streaming, and cavitation microstreaming. In: Ashokkumar M, Cavalieri F, Chemat F, Okitsu K, Sambandam A, Yasui K, Zisu B (eds) Handbook of ultrasonics and sonochemistry. Springer, Singapore
100. Beyer RT (1997) Nonlinear acoustics. Acoustical Society of America, New York
101. Yasui K, Izu N (2017) Effect of evaporation and condensation on a thermoacoustic engine: a Lagrangian simulation approach. J Acoust Soc Am 141:4398–4407. doi:10.1121/1.4985385
102. Nyborg WL (1958) Acoustic streaming near a boundary. J Acoust Soc Am 30:329–339. doi:10.1121/1.1909587
103. Elder SA (1959) Cavitation microstreaming. J Acoust Soc Am 31:54–64. doi:10.1121/1.1907611
104. Mettin R, Cairos C (2016) Bubble dynamics and observations. In: Ashokkumar M, Cavalieri F, Chemat F, Okitsu K, Sambandam A, Yasui K, Zisu B (eds) Handbook of ultrasonics and sonochemistry. Springer, Singapore

http://www.springer.com/978-3-319-68236-5

Acoustic Cavitation and Bubble Dynamics

Yasui, K.

2018, VIII, 124 p. 84 illus., Softcover
ISBN: 978-3-319-68236-5